ACS APPLIED MATERIALS & INTERFACES

www.acsami.org Research Article

GLUT-Targeting Phototherapeutic Nanoparticles for Synergistic Triple Combination Cancer Therapy

Busra Cetin Ersen, Beyza Goncu, Aydan Dag,* and Gokcen Birlik Demirel*

Cite This: *ACS Appl. Mater. Interfaces* 2023, 15, 9080−9098 Read Online

ACCESS | Metrics & More | Article Recommendations | Supporting Information

ABSTRACT: The combination of multimodal therapies into one nanocarrier system is promising for its potential to enhance treatment performance by overcoming the efficacy problems encountered in conventional monomodal therapy. In this study, targeted and multimodal therapeutic hybrid nanocarriers are fabricated for breast cancer treatments. In this context, the synthesized gold nanorods (AuNRd), photothermal therapy (PTT) agent, are coated with doxorubicin (DOX) conjugated, targeted, and biocompatible tetrablock glycopeptide (P(DMAEMA-*b*-HMBAMA-*b*-FrucMA)-*b*-P(Lys)/DOX, P-DOX) polymer. Here, fructose-based (Fruc) glycopeptide polymer enhances cellular uptake into breast cancer through GLUT5. A photosensitizer molecule, indocyanine green (ICG), was loaded into the particles to provide photodynamic therapy (PDT) upon NIR light at 808 nm. In the final step of the fabrication, the polymer-coated nanoparticles are integrated with antisense ISIS5132 oligonucleotides to prevent apoptotic resistance of cells against drug molecules. The biocompatibility and therapeutic efficacy of the nanoparticles are evaluated on both human normal skin fibroblast cell (CCD-1079Sk) and human breast cancer cell (MCF7) lines. These multimodal therapeutic AuNRd@P-DOX/ICG/ISIS5132 nanoparticles demonstrate an efficient triple synergistic effect of chemo-/PTT/PDT, which is desired for breast cancer treatment. We believe that this promising multimodal therapeutic nanoparticle system can promote the further clinical application in the treatment of breast cancer and can also be adapted to other types of cancer.

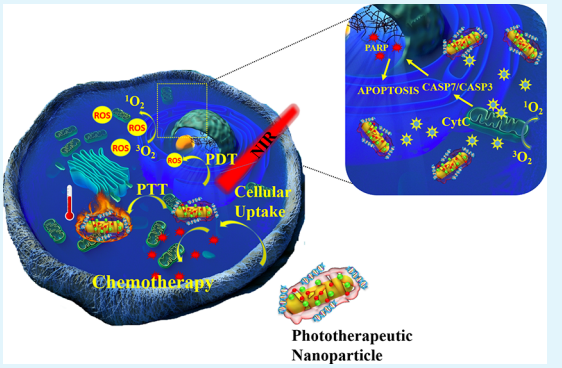

KEYWORDS: *phototherapeutic, NIR, photothermal, photodynamic, chemotherapy, Au nanorod, ISIS5132, GLUT-targeting*

INTRODUCTION

Breast cancer is a type of malignant tumor that seriously threatens women's health and has a high mortality rate in late-phase patients. Chemotherapy, which is the most used traditional unimodal treatment method, has unsatisfying efficacy due to various undesirable properties of chemotherapeutic agents, such as severe toxic side effects, short half-life in blood circulation, low bioavailability, and poor specificity.[1] To overcome these problems, combining different therapeutic methods in one nanocarrier system can provide considerable potential for both fundamental and clinical studies.[2] In this context, two important features should be considered to increase the therapeutic efficacy of nanoparticles. The first is to provide the specific and localized release of cargo molecules from nanocarriers. For this purpose, the nanocarriers are designed with targeted units to specifically direct the particles to the desired tumor location. Targeted nanocarriers accumulate more in the tumor area than in the healthy tissue, thus enhancing the therapeutic efficacy of the nanocarriers. In this respect, selecting of targeting agents is a significant parameter. Thanks to the developments in cancer biology, knowledge of the biological properties of cancer cells is increasing every day. This knowledge helps us to choose the targeting agents that have an affinity against cancer cells without causing harm to healthy cells. It is known that glucose is essential for cancer cell metabolism and it is transported into the cells by glucose transporters, such as GLUT.[3] In this sense, recent studies demonstrated that GLUT5, a specific fructose transporter is overexpressed in breast cancer cells and tissues but is absent in healthy mammary tissues.[4] Therefore, fructose can be used as a therapeutic targeting agent to guide the nanocarrier specifically to breast cancer cells. Zhao et al. synthesized fructose-coated micelles using RAFT polymerization to induce the specific binding between micelles and breast cancer cells instead of normal cell.[4] They reported that fructose-coated micelles were specifically uptaken by breast cancer cells.[4] In a recent study, Zhou et al. synthesized

Received: November 27, 2022
Accepted: February 1, 2023
Published: February 13, 2023

fructose-functionalized liposomes to evaluate the targeting efficacy of fructose moieties both *in vitro* and *in vivo*.[5] They exhibited that fructose-functionalization significantly enhanced the tumor-targeting of liposomes. To enhance the therapeutic efficacy of the targeted-nanocarriers, the other significant issue is to combine the different therapies in one nanocarrier system. Recent studies clearly demonstrated that the traditional single-modal therapies such as chemotherapy are insufficient for many types of cancer treatment. Therefore, the development of multitriggered nanocarriers has an important potential to overcome the limitations mentioned above in traditional methods with the synergetic anticancer effect of the system. Recent studies have shown that the photo-therapeutic nanoplatforms, which combine the photothermal (PTT) and photodynamic therapy (PDT) in one nanocarrier, have become a promising treatment method for various of types of cancer such as breast, skin, head, and neck. In photo-therapeutic nanoplatforms, the near-infrared (NIR) light (600−900 nm) is preferred since it has higher tissue penetration and is less harmful than visible light for healthy tissues.[6] In PTT, NIR light is absorbed by the NIR-responsive phototherapeutic nanomaterials and converted to heat causing selectively cell death ultimately as a result of local hyper-thermia.[7] Among the phototherapeutic nanomaterials, gold nanorods (AuNRd) are widely used as the photothermal conversion agent due to the ease of large-scale synthesis easily and the tunable plasmonic properties in the NIR region by changing synthesis conditions.[8] In addition to the use of AuNRd for photothermal effectivity, they can also be used as the core materials of the multimodal nanocarriers for controlled drug release. It is well known that AuNRd have a strong affinity to thiols. Therefore, this phenomenon is generally used in the functionalization of AuNRd with thiol-modified polymers to obtain multifunctional controlled therapeutic materials.[9] In addition to PTT, PDT is another critical way to kill cancer cells selectively. In PDT, a photosensitizer (PS) molecule is activated by NIR light irradiation to generate cytotoxic reactive oxygen species (ROS). Indocyanine green (ICG), which is an FDA-approved PS molecule, is widely used for phototherapy applications as a PS agent or fluorescent probe.[10] ICG acts as a photothermal agent and photodynamic photosensitizer under 808 nm NIR laser irradiation. However, free ICG has poor stability in physiological solutions and this is a major challenge that needs to be overcome for clinical applications.[11] For this purpose, in general, ICG molecules are encapsulated in a carrier system to get control of the stability of the molecules.[11] Many recent studies have shown that the combining PTT and PDT in a single therapeutic system is crucially important for achieving a high therapeutic index.

Antisense oligonucleotides (ASOs) are investigated in clinical trials for various potential cancer-relevant therapeutic targets. ASO treatment is an attractive strategy for the specific regulation of the expression of genes involved in the pathogenesis of cancer since they are easily applicable with acceptable toxicity profiles. However, their short half-life, instability, nonspecificity, and ionic characteristics hinder their efficiency. One of the strategies to improve the pharmacokinetic properties and increase specific cell-targeting is their association with nanocarriers. Nanocarriers can lead to the controlled release of ASOs and provide benefits such as the prevention of degradation, targeting delivery, multifunctionality, and bioimaging. Recent studies have demonstrated that ASOs can be easily applied in combination with chemotherapeutic agents. Since the early 1990s, RAF proteins function predicted to provide effective treatment for various cancers.[12] The RAF modulates the development and metastasis of various cancer types including breast cancer.[13] Raf-1 is an oncoprotein, and several oligonucleotides aim to decrease its expression, including ISIS3521.[14] Particularly, ISIS5132, a 20-base phosphorothioate oligonucleotide, has been demonstrated to suppress c-Raf-1 expression, and several clinical trials precisely reported that the efficacy and toxicity depend on the duration of administration.[15,12]

Herein, we report a strategy to fabricate multimodal and multifunctional hybrid core/shell AuNRd@P-DOX/ICG/ISIS5132 nanoparticles for the synergistic effect of the combination of chemo-/photothermal-/photodynamic therapies for the treatment of breast cancer *in vitro*. In this study, AuNRd, ICG, and DOX were used for theranostic probes. AuNRd serve as a photothermal agent due to their high-photothermal conversion efficiency and strong near-infrared absorption. ICG plays an important role both as a photothermal agent and ROS generator. Meanwhile, we synthesized fructose-targeted and DOX-conjugated tetra-block copolymers (P-DOX) as polymer shells of the particles. Further, AuNRd@P-DOX/ICG particles were conjugated with ISIS5132, a specific antisense-oligonucleotide sequence that serves to enhance the selective apoptosis of breast cancer cells. This theranostic nanoparticle system exhibited not only excellent tumor selectivity and but also demonstrated great synergistic therapy potential by combining chemotherapy, PTT and PDT, and in a single theranostic nanosystem.

EXPERIMENTAL SECTION/METHODS

Materials. Hexadecyltrimethylammonium bromide (CTAB, ≥98%), tetrachloroauric(III) acid trihydrate (99%), L-ascorbic acid (AA, 99%), silver nitrate (ACS reagent, ≥99.0%), sodium borohydride (reagent plus, 99%), 4-hydroxybenzaldehyde (98%), 6-bromo-hekzanol (97%), L-lysine (≥97%), 4-(dimethylamino) pyridine (DMAP, purum, ≥98.0%), dicyclohexylcarbodiimide (DCC, 99%), triethylamine (Et_3N, ≥99%), sodium azide (≥99.5%), 3-bromopropylamine hydrobromide (98%), methacryloyl chloride (97%), D-fructose (≥99%), tetrahydrofuran (THF, for analysis EMSURE ACS, Reag. Ph Eur), triphosgene (reagent grade, 98%), tetrabutylammonium fluoride (TBAF, 1.0 M in THF), trifluoroacetic acid (≥99), and 2-(dimethylamino)ethyl methacrylate (DMAEMA, 98%) were all from Sigma-Aldrich. 2,2′-Azobis(2-methylpropionitrile) (AIBN, Sigma-Aldrich) was recrystallized twice from methanol (MeOH) and stored at −18 °C. *tert*-Butyl alcohol (ACS, ≥99%), di-*tert*-butyl dicarbonate (≥97%), and 3-(trimethylsilyl) propargyl alcohol (≥98%) were purchased from Alfa Aesar. Deionize water (DIW) was produced by a Milli-Q reverse osmosis system and had a resistivity of 18.2 MΩ·cm. All solvents for synthesis were obtained from Sigma-Aldrich and used without further purification.

Synthesis of Precursor Compounds. 1-Azido-3-amino propane,[16] trimethylsilyl-protected alkyne-functional RAFT agent (CPADB-TMS),[17] 3-*O*-methacryloyl-2,3:4,5-di-*O*-isopropylidene-β-D-fructopyranose (*ipr*-FrucMA) 4-((6-hydroxyhexyl)oxy)-benzaldehyde methacrylate (HBAMA),[16] and *N*-*N*-di-*tert*-butoxycarbonyl-L-lysine-*N*-carboxyanhydride (*tBoc*-Lys-NCA)[18] were synthesized according to published procedures.

SYNTHESIS OF POLYMERS

Preparation of P(*ipr*-FrucMA)-TMS Homoblock Polymer (P1). P(*ipr*-FrucMA) was synthesized as described in the literature.[17] *ipr*-FrucMA (2.00 g) (6.09 mmol, 50 equiv), 5 mL of toluene, 47.42 mg of CPADB-TMS (0.12 mmol, 1.00

https://doi.org/10.1021/acsami.2c21180
ACS Appl. Mater. Interfaces 2023, 15, 9080−9098

equiv), and 2.50 mg of AIBN (15.21 μmol, 0.125 equiv) were placed in a dry 10 mL of a glass vial with a septum cap. The polymerization mixture was degassed by purging nitrogen through the reaction mixture for 50 min and then placed in an oil bath thermostated at 70 °C. The reaction mixture was stirred at room temperature for 9 h; after which, the solvent was removed in a vacuum. The resulting product was dissolved in THF, and the polymer was precipitated two times into hexane, isolated as a pale pink solid, and dried in a vacuum at 40 °C. The molecular weight of P(*ipr*-FrucMA)-TMS (P1) was determined by ^{1}H-NMR and GPC analysis. (Figures S1A and S5A) ^{1}H-NMR (500 MHz, $CDCl_3$, δ ppm): 7.99−7.37 (m, 5H, $-C_6H_5$), 5.25−3.25 (bm, 7H, repeating unit of *ipr*-FrucMA), 1.59, (s 3H, $CH(CH_3)$) 1.50−1.25 (m, 12H, $OC(CH_3)_2$), 0.19 (s, 9H, Si-$(CH_3)_3$).

Preparation of P(*ipr*-FrucMA-*b*-HBAMA)-TMS Diblock Copolymer (P2). Previously synthesized P(*ipr*-FrucMA)-TMS was used as a Macro-RAFT agent. P(*ipr*-FrucMA) (1.00 g) (0.07 mmol, $M_{n,NMR}$ = 14.5 kDa, 1 equiv), 5.85 mL of toluene, 0.60 g of HBAMA (2.07 mmol, 30 equiv), and 1.41 mg of AIBN (8.62 μmol, 0.125 equiv) were placed in a dry 10 mL of glass vial with a septum cap. The polymerization mixture was degassed by purging nitrogen through the reaction mixture for 50 min and then placed in an oil bath thermostated at 70 °C. After 6 h, excess toluene was removed by rotary evaporation, and the resulting homopolymer P(*ipr*-FrucMA-*b*-HBAMA)-TMS was recovered by precipitation in hexane twice. The diblock copolymer was dried under a vacuum at 40 °C. The molecular weight of P(*ipr*-FrucMA-*b*-HBAMA)-TMS) (P2) was determined by GPC and ^{1}H-NMR spectroscopy. (Figures S1B and S5A). ^{1}H-NMR (500 MHz, $CDCl_3$, δ ppm): 7.99−7.37 (m, 5H, $-C_6H_5$), 5.25−3.25 (bm, 7H, repeating unit of *ipr*-FrucMA), 1.59(s, 3H, $CH(CH_3)$) 1.50−1.25 (m, 12H, $OC(CH_3)_2$), 0.19 (s, 9H, Si-$(CH_3)_3$).

Preparation of P(*ipr*-FrucMA-*b*-HBAMA-*b*-DMAEMA) Triblock Copolymer (P4). P(*ipr*-FrucMA-*b*-HBAMA)-TMS was applied as a Macro-RAFT agent to synthesize a triblock copolymer. DMAEMA (0.58 mL) (3.92 mmol, 70 equiv), 5 mL of toluene, 1.20 g of P(*ipr*-FrucMA-*b*-HBAMA)-TMS (0.05 mmol, $M_{n,NMR}$ = 21.25 kDa, 1.00 equiv), 4 mL of 1,4-dioxane, and 1.38 mg of AIBN (8.41 μmol, 0.15 equiv) were placed in a dry 10 mL glass vial with a septum cap. The polymerization mixture was degassed by purging nitrogen through the reaction mixture for 50 min and then placed in an oil bath thermostated at 70 °C. The reaction mixture was stirred at room temperature for 6 h, after which the solvent was removed in a vacuum. The resulting product was dissolved in THF, and the polymer was precipitated two times into hexane, isolated as a pale pink solid, and dried in a vacuum at 40 °C. The molecular weight of P(*ipr*-FrucMA-*b*-HBAMA-*b*-DMAEMA)-TMS (P3) was determined by ^{1}H-NMR and GPC spectroscopy. (Figures S1C and S5A) ^{1}H-NMR (500 MHz, $CDCl_3$, δ ppm): 9.85 (s, −CHO from HBAMA), 7.80 and 6.95 (bs, $-C_6H_4$ from HBAMA), 5.25−3.25 (bm, 7H, repeating unit of *ipr*-FrucMA, and 4H, repeating unit of HBAMA $-OCH_2$) and 2H repeating unit of DMAEMA $-OCH_2$), 2.58 (s, 2H repeating unit of DMAEMA $-NCH_2$), 0.19 (s, 9H, Si-$(CH_3)_3$).

After that, the TMS group was removed from the P(*ipr*-FrucMA-*b*-HBAMA-*b*-DMAEMA)-TMS (P3) triblock copolymer through basic hydrolysis, affording the P(*ipr*-FrucMA-*b*-HBAMA-*b*-DMAEMA) triblock copolymer. In a typical procedure, TMS-terminated triblock copolymer (0.75 g, 25.97 μmol, $M_{n,NMR}$ = 29.90 kDa) was dissolved in 45 mL of THF (HPLC grade) under N_2, and tetrabutylammonium fluoride (TBAF) (87 μL, 87 μmol) was added. The reaction mixture was stirred for 3 h and then passed through a neutral aluminum oxide column. The crude product, P(*ipr*-FrucMA-*b*-HBAMA-*b*-DMAEMA) (P4), is concentrated *in vacuo* and precipitated in hexane twice. ^{1}H-NMR (500 MHz, $CDCl_3$, δ ppm): 9.85 (s, −CHO from HBAMA), 7.80 and 6.95 (bs, $-C_6H_4$ from HBAMA), 5.25−3.25 (bm, 7H, repeating unit of *ipr*-FrucMA, and 4H, repeating unit of HBAMA $-OCH_2$) and 2H repeating unit of DMAEMA $-OCH_2$), 2.58 (s, 2H repeating unit of DMAEMA $-NCH_2$) (Figure S2A).

Preparation of Azido End Functional P(*tBoc*-Lys) (P5). A flame-dried 25 mL Schlenk flask was charged with 1.00 mg of *tBoc*-Lys-NCA (3.67 mmol, 50.00 equiv) and dissolved in 10 mL of dry DMF. After 10 min of magnetic stirring under an argon atmosphere, 7.51 μL of 1-azido-3-amino propane (0.07 mmol, 1.00 equiv) was added to the reaction mixture in one portion. The mixture was stirred for 96 h at 0 °C. Subsequently, the DMF was evaporated and the polymer was recovered by precipitation in diethyl ether resulting in a white powder after filtration and drying at room temperature under a vacuum. The obtained powder was stored at −80 °C prior to use. The molecular weight of P(*tBoc*-Lys) was determined by GPC-MALS and ^{1}H-NMR spectroscopy. (Figures S5B and S2B) ^{1}H-NMR (500 MHz, DMSO-d_6, δ ppm): 8.20 (bs, 1H, repeating unit of *tBoc*-Lys, CHNH), 6.65 (bs, 1H, repeating unit of *tBoc*-Lys, CH_2NH), 3.78 (bs, 2H, repeating unit of *tBoc*-Lys, CH_2NH)), 2.87 (bs, 2H, repeating unit of *tBoc*-Lys, CH_2CH_2NH), 0.19 (m, 9H, repeating unit of *tBoc*-Lys, *tBoc* and 6H, repeating unit of *tBoc*-Lys $CH_2CH_2CH_2$).

Preparation of P(*ipr*-FrucMA-*b*-HBAMA-*b*-DMAEMA)-*b*-P(*t*Boc-Lys) Tetrablock Copolymer via Click Reaction (P6). A click reaction procedure is as follows: 0.56 g of P(*ipr*-FrucMA-*b*-HBAMA-*b*-DMAEMA) (18.79 mmol, $M_{n,NMR}$ = 29.80 kDa, 1 equiv), 0.125 g of P(*tBoc*-Lys) (20.67 mmol, 1.1 equiv), 39 μL of PMDETA (0.188 mol, 10 equiv), and 13.47 mg of CuBr (93.96 mmol, 5 equiv) were placed in a Schlenk flask, degassed by three freeze-pump thaw cycles, backfilled with nitrogen, sealed, and stirred in an oil bath at 40 °C for 2 days. The crude product was passed through a neutral alumina column to remove copper complexes and recovered by precipitation twice in hexane. The crude polymer was also dialyzed for 48 h (molecular weight cutoff, MWCO 3.5 kDa) against deionized water and was transferred to THF for another 24 h. Then, the residue was collected by evaporation and analyzed by ^{1}H-NMR measurements (Figure S2C).

Hydrolysis of P(FrucMA-*b*-HBAMA-*b*-DMAEMA)-*b*-P-(Lys) Tetrablock Copolymer (P7). P(*ipr*-FrucMA-*b*-HBAMA-*b*-DMAEMA)-*b*-P(*tBoc*-Lys) (0.50 g) was placed in a flask, after the addition of the $CHCl_3$:DIW mix (3 mL:350 μL), and then placed into an ice bath for 30 min under nitrogen flow. Then, 650 μL of trifluoroacetic acid (TFA) was added into the round-bottomed flask to carry out hydrolysis and the reaction was stirred overnight at room temperature. Subsequently, the solution of hydrolysate was dialyzed for 1 day (MWCO 3.5 kDa) against UP water. Then, the purified P(FrucMA-*b*-HBAMA-*b*-DMAEMA)-*b*-P(Lys) (P7) tetrablock copolymer was collected by lyophilization and analyzed by ^{1}H-NMR and GPC measurements. (Figures S3A and S5B).

Preparation of DOX Conjugated P(FrucMA-*b*-HBAMA-*b*-DMAEMA)-*b*-P(Lys) Tetrablock Copolymer (P-DOX). Doxorubicin·HCl (DOX) (0.032 g) (1.2 equiv for

https://doi.org/10.1021/acsami.2c21180
ACS Appl. Mater. Interfaces 2023, 15, 9080−9098

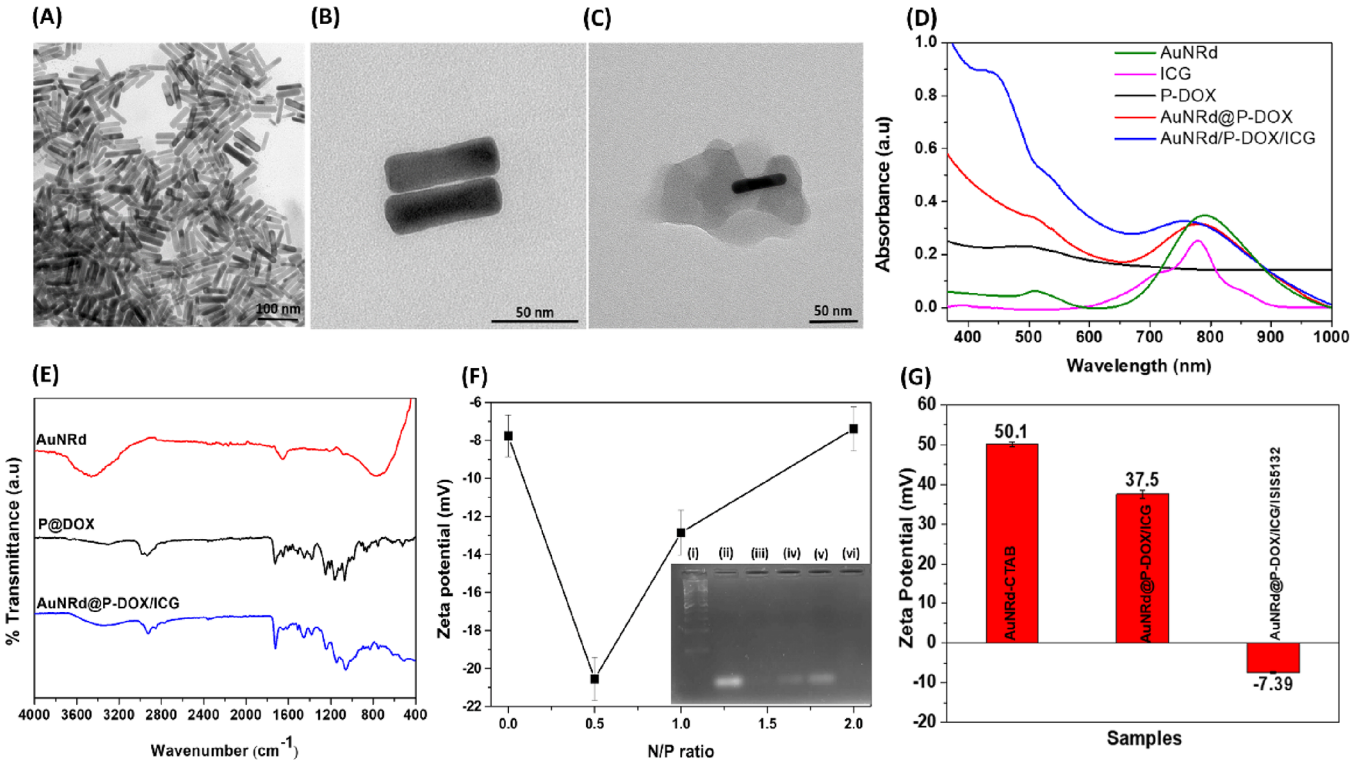

Figure 1. TEM images of (A) AuNRd, (B) high-resolution TEM image of AuNRd, (C) AuNRd@P-DOX/ICG nanoparticles, (D) UV−vis spectra of particle components; (E) ATR-FTIR spectra of AuNRd@P-DOX/ICG and its precursors; (F) zeta potential values of AuNRd@P-DOX/ICG/ISIS5132 at different N/P ratios (inserted image: agarose gel electrophoresis of AuNRd@P-DOX/ICG/ISIS5132 at different N/P ratios; (i) ladder, (ii) ISIS5132, (iii) N/P = 2/1, (iv) N/P = 1/1, (v) N/P = 0.5/1, (vi) Free NP); and (G) zeta potential values of AuNRd, AuNRd@P-DOX/ICG, and AuNRd@P-DOX/ICG/ISIS5132 nanoparticles.

each aldehyde unit) was dissolved in 2 mL of DMSO, and then P(FrucMA-*b*-HBAMA-*b*-DMAEMA)-*b*-P(Lys), 50 mg, 1.63 μmol, 1 equiv) was added into the mixture in the presence of 6 μL of Et_3N. The reaction mixture was stirred overnight. Subsequently, the Dox-conjugated tetrablock copolymer solution was purified using the dialysis procedures. The solution was transferred into a dialysis bag (MWCO 3.5 kDa) and dialyzed against DI water for 48 h, and the residue collected by lyophilization gave a red flocculent product. The obtained P(FrucMA-*b*-HBAMA-*b*-DMAEMA)-*b*-P(Lys)-DOX (P-DOX) was analyzed by ^{1}H-NMR and GPC measurements (Figures S3B and S5C).

Synthesis and Characterization of AuNRd. AuNRd were synthesized following previously described seed-mediated protocol.[19] First, the seed solution was prepared. For this purpose, 0.125 mL of 0.01 M $HAuCl_4$ was added to 4.88 mL of 0.1 M CTAB solution and then 0.6 mL of 0.01 M $NaBH_4$ (ice cold) was added to the mixture. The solution was vigorously stirred for 2 min, while the color of the solution turned brownish-yellow. This seed solution was kept in a water bath at 25 °C for 2 h. The growth solution was prepared using the following procedure. First, 2.5 mL of 0.01 M $HAuCl_4$ and 0.5 mL of 0.01 M $AgNO_3$ (0.01 M) were gently mixed in 50 mL of 0.1 M CTAB solution. Then, 1 mL of 1 M HCl and 0.4 mL of 0.1 M AA were added to the growth solution under stirring gently. Finally, 0.125 mL of the seed solution was added to the growth solution and followed by vigorous stirring. The mixed solution was aged at rt overnight. The AuNRd were characterized by TEM and UV−vis spectroscopy (Figure 1A,B,D).

Synthesis of Phototherapeutic AuNRd@P-DOX Nanoparticles. First, CTA-ended polymer chains were transformed into thiol chain ends by a well-known reduction method using $NaBH_4$.[20] The tetrablock polymer solution (0.3 g in 5 mL DIW) was prepared, and $NaBH_4$ (1 M) in DIW (5 mL) was added to the solution dropwise via a syringe. The mixture was continuously stirred in darkness at rt for 12 h. The product was dialyzed (MWCO 3.5 kDa) against deionized H_2O in darkness at rt for another 2 days. After that, the thiolated polymer solution was added to the solution of AuNRd (3.5 mL) dropwise via a syringe. The AuNRd:thiolated-polymer mole ratio was kept at 10:1. The mixture was stirred in darkness overnight and at rt. The resulting AuNRd@P-DOX nanoparticles were collected by a centrifuge, resuspended with DIW, and freeze-dried. The AuNRd@P-DOX were stored at 4 °C.

Preparation of ICG-Loaded AuNRd@P-DOX/ICG Nanoparticles. Briefly, AuNRd@P-DOX (20 mg) was dispersed in 10 mL of DIW. Then, 1 mL of ICG solution (1 mg/mL in DIW) was added drop by drop under stirring and the resulting solution was stirred at room temperature overnight at dark.[21] Then, ICG-loaded particles were centrifuged and freeze-dried. The drug loading content (DLC) of the prepared AuNRd@P-DOX/ICG was determined by a UV−vis spectrophotometer. Briefly, a certain amount of freeze-dried AuNRd@P-DOX/ICG NPs was dispersed in DIW, and the amount of ICG was determined by a UV−vis spectrophotometer at 795 nm. The drug loading content (DLC) was calculated as

https://doi.org/10.1021/acsami.2c21180
ACS Appl. Mater. Interfaces 2023, 15, 9080−9098

$$\mathrm{DLC}(\%) = (\mathrm{Wt}\ (\mathrm{ICG} - \mathrm{loaded\ NPs})/\mathrm{Wt}\ (\mathrm{loaded\ ICG})) \times 100\%$$

where Wt (loaded ICG) is the weight of the loaded ICG and Wt (ICG-loaded NCs) is the weight of ICG-loaded NPs.

The encapsulation efficiency (EE) was calculated as

$$\mathrm{EE}(\%) = (\mathrm{Wt}\ (\mathrm{feeding\ ICG})/\mathrm{Wt}\ (\mathrm{loaded\ ICG})) \times 100\%$$

where Wt (loaded ICG) is the weight of the loaded ICG and Wt (feeding ICG) is the weight of the feeding ICG.

Preparation of ISIS5132 Oligonucleotide-Conjugated AuNRd@P-DOX/ICG/ISIS5132 Nanoparticles. AuNRd@P-DOX/ICG/ISIS5132 conjugates were prepared by adding predetermined amounts of either Cy3- or Cy5-tagged ISIS5132 (0.152 mM/L) into the AuNRd@P-DOX/ICG (1 mg/mL). The mixture was stirred at room temperature for 1 h. AuNRd@P-DOX/ICG/ISIS5132 conjugates were formed at various nitrogen/phosphorus (N/P) ratios (0.5/1, 1/1, 2/1).[18] Then, the complexation ability of nanoparticles was assessed by agarose gel electrophoresis. Electrophoresis was carried out on a 2.5% agarose gel with a current of 50 V for 45 min in a TAE buffer solution (2% Tris HCl, 1% acetic acid, and 1 mM EDTA). Free ISIS5132 was loaded as a reference. The retardation of the complexes was visualized by an ethidium bromide staining. An ethidium bromide staining visualized the retardation of the complexes. The images were obtained by a Fusion Fx7 (Vilber Lourmat, Collégien, France).

IN VITRO DOX RELEASE STUDY

DOX-conjugated tetrablock copolymer (P(FrucMA-*b*-HBAMA-*b*-DMAEMA)-*b*-P(Lys), P-DOX, 5 mg) was dissolved in PBS solution (5 mL) and filled into a dialysis bag (MWCO 1 kDa). After that, the bag was placed into 50.0 mL of buffer solution (pH = 5.5, 6.8, and 7.4) at 37 °C within an orbital shaker. At different predetermined time intervals, 2.5 mL of the suspension was drawn and replaced by fresh PBS solution (2.5 mL) to continue the DOX release study. The DOX concentration in the suspension was determined by UV−vis spectroscopy. The absorbance was measured at a wavelength of 488 nm. The DOX-release efficiency was converted by the DOX standard curve equation. To compare the release efficiency of DOX from P-DOX, the same procedure was repeated for AuNRd@P-DOX.

Photothermal Performance of Particles. To reveal the photothermal effects of AuNRd and AuNRd@P-DOX/ICG nanoparticles under 808 nm, NIR laser irradiation was examined into PBS solution (pH = 7.4) in quartz cuvettes (1 mg/mL) as a function of irradiation time and irradiation intensity. Temperature changes were recorded by a thermal camera (FLIR Ex-8).

Photothermal Conversion of Nanoparticles. The photothermal conversion efficiency (η) of the AuNRd@P-DOX/ICG/ISIS5132 nanoparticles was calculated using the following eqs 1−4.[22] For this purpose, the temperature changes of the nanoparticle solution (62.5 μg/mL) were recorded as a function of time under 0.75 W/cm^2 808 nm NIR laser irradiation until the temperature value reached a steady state (5 min). First, we calculated the photothermal conversion efficiency (η) from eq 1 as previously reported;[22]

$$\eta = \frac{hS(T_{\max} - T_{\max,H_2O}) - Q_o}{I(1 - 10^{-A_\lambda})} \quad (1)$$

$$\theta = \frac{(T - T_{\mathrm{surr}})}{(T_{\max} - T_{\mathrm{surr}})} \quad (2)$$

$$hs = \frac{mC_p}{\tau_s} \quad (3)$$

$$t \equiv -\tau_s \ln \theta \quad (4)$$

where Q_0 is the heat dissipated from the light absorbed by the quartz cuvette and DI water, h is a heat transfer coefficient, S is the surface area of the quartz cuvette, I is the laser incident power (0.75 W/cm^2), A_λ (0.4) is the absorbance intensity of nanoparticles at 808 nm, $T_{\max}$ (45 °C) and $T_{\max,H2O}$ (23.2 °C) are the maximum equilibrium temperatures of quartz cuvette cells containing nanoparticles and DI water, respectively. hS was calculated by using eq 2[22] where C_p (4.2 J/°C) and m (0.5 g) are heat capacity and the mass and of water, respectively. To calculate hS, first, θ was calculated using eq 3 where T is the nanoparticle solution temperature, and T_{surr} is the ambient temperature of the surrounding, which is 21.7 °C. Thus, the time constant of heat transfer (τ_s) can be calculated using eq 4. From these calculations, τ_s and η were determined to be 171 s and 57.7%, respectively.

IN VITRO STUDIES

Cell Culture. MCF7 cells grown in a DMEM/F12 medium (Gibco, Thermo Fisher Scientific, MA, USA) were supplemented with 10% FBS (Gibco), 1% penicillin−streptomycin (Gibco). Cultures were incubated at 37 °C in a 5% CO_2 atmosphere and 95% relative humidity. All *in vitro* assays were performed under the same cultivation conditions, and the entire study was completed passages between 11 and 29 for MCF7 cells and passages between 21 and 25 for CCD-1079Sk cells. Each assay was performed in triplicates throughout the study.

***In Vitro* Cytotoxicity.** In this assay, the tetrazolium salt 3-(4,5-dimethyl-2-thiazolyl)-2,5-diphenyl-2*H*-tetrazolium bromide, Thermo Fisher Scientific, NY, USA) is yellow and is easily incorporated by viable cells and reduced by the mitochondrial enzyme succinate dehydrogenase to the formazan compound, which is purple.

Dark-cytotoxicity. MCF-7 and CCD-1079Sk cells were seeded in a 96-well plate (density of 8×10^3 cells per well) in a 5% CO_2 atmosphere for 24 h at 37 °C. Then, the AuNRd@P, AuNRd@P/ICG, AuNRd@P-DOX, AuNRd@P-DOX/ICG, AuNRd@P/ISIS5132, AuNRd@P/ICG/ISIS5132, AuNRd@P-DOX/ISIS5132, and AuNRd@P-DOX/ICG/ISIS5132 nanoparticles dispersed in DMEM/F12 with 10 different concentrations (125, 62.5, 31.25, 15.62, 7.81, 3.9, 1.95, 0.97, and 0.24 μg/mL). Cells were incubated for 24 h. The cells were washed with PBS three times to remove residual samples before a fresh cell culture medium was injected into the wells. The stock MTT solution was diluted at 1:10 with a DMEM/F12 medium (without phenol red and FBS). The cells were incubated with the diluted MTT solution (0.1 mL/well) at 37 °C and 5% CO_2 for 4 h. DMSO was added (0.1 mL/well) to solubilize the formazan crystals. The plates were gently agitated and incubated for another 10 min. The absorbance of the supernatant was measured at 570 nm. The outcome was analyzed as described previously.[23] Two noncytotoxic concentrations were chosen for the further experiments based on MTT analyses. All experiments were performed as triplicates/treatments.

https://doi.org/10.1021/acsami.2c21180
ACS Appl. Mater. Interfaces 2023, 15, 9080−9098

Photo-cytotoxicity. MCF-7 and CCD-1079Sk cells were handled as the above procedures. Photo-toxicity group; included with six different consecutive concentrations (62.5, 31.25, 15.62, 7.81, and 3.9 μg/mL) for DOX, AuNRd@P, AuNRd@P/ICG/ISIS5132, and AuNRd@P-DOX/ICG/ISIS5132 with/without NIR exposure after 24 h of treatment. The cells were washed 1× PBS three times to remove residual nanoparticles before adding a fresh cell culture medium. Then, each well was exposed to an 808 nm laser (0.75 W/cm^2) for 5 min. NIR exposure was performed at the 6th hour of treatment. Statistical analyzes were performed to compare the differences between viability and IC_{50} values. IC_{50} values were calculated using a four-parameter logistic regression model by a Quest Graph IC_{50} Calculator.[24]

CELLULAR INTERNALIZATION

To evaluate the targeting specificity and internalization efficiency, the cellular uptake was quantitatively analyzed on both MCF7 and CCD-1079Sk cells.

Both cell lines were treated with AuNRd@P, AuNRd@P/ICG, AuNRd@P-DOX, AuNRd@P-DOX/ICG, AuNRd@P/ISIS5132, AuNRd@P/ICG/ISIS5132, AuNRd@P-DOX/ISIS5132, AuNRd@P-DOX/ICG/ISIS5132, and free DOX (IC_{50}) for 6, 12, and 24 h at two different concentrations (31.25 and 7.8 μg/mL). All of the outcomes were compared with the untreated group. After incubation, the cells were washed and collected by trypsinization for flow cytometric determination of cellular internalization. Cells were resuspended in 1× PBS containing 0.01 mg/mL DAPI to quench the fluorescence of viable cells. Samples were analyzed by flow cytometry (BD Accuri C6), and 10.000 events were performed for each sample. All of the outcomes were compared with the untreated group. Cellular internalization efficiency of nanoparticles on CCD-1079Sk cell lines is explained in Figure S8C.

Additionally, intracellular distributions were visualized by using an inverted fluorescence microscope (ZEISS, Oberkochen, Germany). Incubation for 12 h with AuNRd@P, AuNRd@P/ICG/ISIS5132, and AuNRd@P-DOX/ICG/ISIS5132 with the determined concentrations of the nanoparticles (3.9, 0.97, and 0.24 μg/mL) was performed. This assay is based on the observing internalized nanoparticles in viable cells (DAPI for viable cells shown in blue, ex:359/em:457 nm). The ISIS5132 oligonucleotide was conjugated with Cy3 (ex:548−552/em:562−570 nm) for cases where DOX (ex:595/em:470 nm) could not be detected due to the very low doses in the selected treatment concentrations of nanoparticles.

Quantification of cellular uptake of hybrid nanocarriers was also demonstrated via ICP-MS analysis (Agilent, USA).

WOUND HEALING ASSAY

Before any treatment, a linear scratch was generated with a sterile pipette tip in the monolayer when MCF7 cells were confluent in a 24-well plate. Cellular debris was removed by washing three times with 1× PBS and replaced with DMEM/F12 complete medium containing the DOX (IC_{50}), AuNRd@P, AuNRd@P/ICG, AuNRd@P-DOX, AuNRd@P-DOX/ICG, AuNRd@P/ISIS5132, AuNRd@P/ICG/ISIS5132, AuNRd@P-DOX/ISIS5132, AuNRd@P-DOX/ICG/ISIS5132, and carried DOX amount for the indicated nanoparticle concentrations. The complete medium without the nanoparticle solution served as a negative control (untreated). The light microscope images were acquired by using a microscope lens adapter for smartphones and each scale coordinates were used for microscope centering for each time interval/group. Images were taken at a 4× magnification before treatment (on day 0). After the treatment, plates were incubated at 37 °C with 5% CO_2. The images acquired at 24 and 48 h from each well were further analyzed quantitatively by using ImageJ.[24] The cell quantity of each scratch area was determined[25] by comparing the images between time intervals. The migration was determined by the number of proliferating cells in the scratch area to evaluate proliferation status and precise wound closure capacity after treatment and NIR exposure.

CELL MOTILITY ASSAY

Following the treatment, the cells were stained with calcein AM (Biolegend, CA, USA) for 15 min at 37 °C for live-cell fluorescent tracking. After incubation, cells were washed with 1× PBS, resuspended in phenol-red free DMEM/F12 media, and then imaged using an inverted fluorescence microscope (ZEISS, Oberkochen, Germany).

WESTERN BLOTTING

Total protein lysates were prepared, and total protein concentrations were determined as described previously. An 80 μg total protein lysate was prepared with a 4× laemmli sample buffer and separated on 4−12% handmade polyacrylamide gels. Proteins were transferred to 0.2 μm PVDF membranes (Bio-Rad, USA) in a 1× transfer buffer at 2.5 A for 10 min with the Trans-Blot Turbo Transfer System (Bio-Rad, USA). The membranes were blocked overnight at +4 °C with TBST (tris buffered saline with 0.02% Tween-20) containing 5% nonfat milk. The primary antibodies for Caspase-3, Caspase-7, and PARP were rabbit polyclonal antibodies (dilution 1:2000, Cell Signaling, MA, USA); as normalization control, the GAPDH and B-actin were used to provide a more thorough assessment of sample loading, and antibodies were mouse HRP-conjugated antibody (1:3000, Abclonal, MA, USA), and the secondary antibody that was used was anti-rabbit IgG HRP-linked Antibody (1:2000 dilution, Cell Signaling, MA, USA). The membranes were washed five times for 5 min per wash, each between antibody incubations with TBST. The blots were developed using the ECL detection kit (Advansta, CA, USA) by Fusion Fx7 (Vilber Lourmat, Collégien, France). In chemiluminescence imaging, the membranes were evaluated with the same exposure times for each variable.

INTRACELLULAR ROS DETECTION

The level of the cytosolic and mitochondrial ROS level was quantified by using MitoSOX Red dye (Thermo Fisher Scientific, MA, USA) according to the manufacturer's instructions. The cells were seeded in 50 × 10^3 cells into three consecutive wells in 24-well plates for two-time intervals (24 and 48 h), respectively. The cells were then treated with free DOX (IC_{50}), AuNRd@P/ICG/ISIS5132, AuNRd@P-DOX/ICG/ISIS5132, and carried DOX. Then, the cells were washed three times with cold 1× PBS and replenished with a fresh medium, followed by irradiation with 808 nm laser at 0.75 W/cm^2 for 5 min. After that, the cells were stained by adding 2.5 μM MitoSOX in 1× Hanks' balanced salt solution. After 30 min incubation in the dark, the cells were rinsed three

https://doi.org/10.1021/acsami.2c21180
ACS Appl. Mater. Interfaces 2023, 15, 9080−9098

Scheme 1. Schematic Illustration of the Preparing Multifunctional AuNRd@P-DOX/ICG/ISIS5132 Phototherapeutic Nanoparticles and Application in Synergistic Combination Cancer Cell Therapy

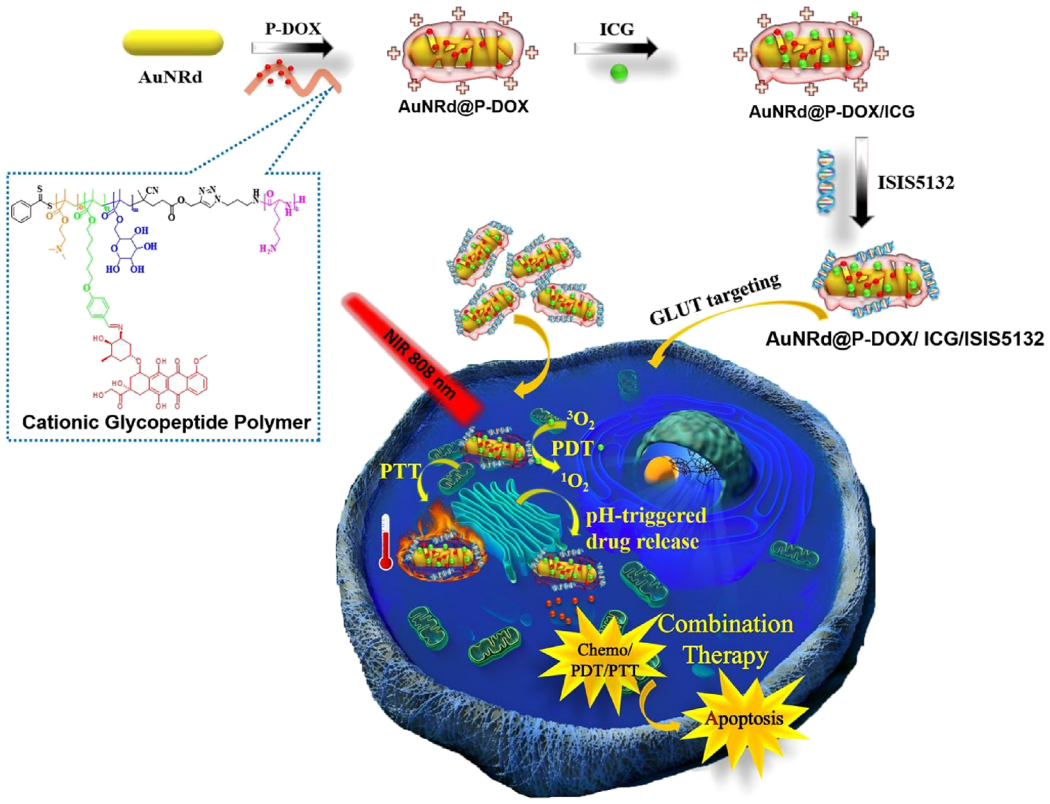

times with PBS and stained for nuclei visualization by DAPI. Intracellular ROS intensity detection was analyzed with an inverted fluorescence microscope (ZEISS, Oberkochen, Germany).

APOPTOSIS ASSAY

Apoptosis analyses were performed with an FITC-conjugated Annexin V Apoptosis Detection Kit containing PI (Biolegends, CA, USA) according to the manufacturer's instruction by using the BD Accuri C6 flow cytometry system (BD Biosciences, NJ, USA). A total of 50 × 10^3 cells/mL was seeded in 24-well plates, and after 24 h, cells were treated with nanoparticles with or without NIR exposure for 24 and 48 h. All experiments were performed in triplicates. Then, cells were suspended, scraped, and pelleted by centrifugation. A 100 mL suspension of cells was mixed with an assay reagent and incubated for 20 min in the dark at room temperature. The gating was adjusted according to the untreated sample, and the results were presented as the percentage of cells that were viable (Ann-V^- PI^-), early apoptotic (Ann-V^+ PI^-), late apoptotic (Ann-V^+ PI^+), or dead (Ann-V^- PI^+).

STATISTICAL ANALYSIS

All data were normalized by their respective controls and are presented as mean ± standard error of the mean for each treatment group. All graphs and analyses were carried out by using GraphPad Prism 9.3. $P < 0.05$ was considered sufficient to reject the null hypothesis, and asterisks represent different levels of significance; *$p < 0.05$, **$p < 0.01$, ***$p < 0.001$, and ****$p < 0.0001$. All of the experiments were triplicated and repeated at least three times. The student's *t*-test (two-tailed) and or Mann–Whitney U-tests were performed to test the significance of the differences between the two groups when necessary between time intervals or NIR treatment or different concentration groups. Comparisons among groups were performed using one-way analysis of variation (ANOVA) and/or two-way ANOVA with multiple comparison tests following Tukey's, Sidak's, and Dunnett's tests. Bonferroni corrections were applied for multiple comparisons when necessary. A two-factor ANOVA was utilized for cell distribution and fluorescence from the microscope images; a two-factor ANOVA was utilized followed by a post-hoc analysis for intensity. Microscope images were analyzed by using four images from two independent experiments. All of the flow cytometry analyzes were conducted using BD Accuri C6 software. Statistical testing for multiple comparisons from western blot experiments and an estimation is performed for type-I error rates by False Discovery Rate (FDR) by Benjamini and Hochberg methods, Q accepted as 3%.[26]

RESULTS AND DISCUSSION

Design and Characterization of the Phototherapeutic Hybrid Nanoparticles. AuNRd were synthesized following the seed-mediated template-assisted protocol with some modifications. As seen in the TEM image, AuNRd exhibit good uniformity with a length of 67 ± 3.6 nm and a width of 20.3 ± 1.2 nm (Figure 1A,B). The average aspect ratios of the AuNRd were calculated to be 3.5 from TEM images, which is suitable for 808 nm NIR irradiation. We aim to develop a multifunctional phototherapeutic nanoparticle system for the synergetic cancer therapy. For this purpose, AuNRd were functionalized with DOX-conjugated cationic glycopeptide tetrablock polymer (P-DOX). It is well known that the design of the polymer layer is an essential key for developing a

https://doi.org/10.1021/acsami.2c21180
ACS Appl. Mater. Interfaces 2023, 15, 9080−9098

targeted and multifunctional therapeutic core/shell nanoparticle system. For this reason, we synthesized the DOX-conjugated cationic glycopeptide tetrablock P(FrucMA-*b*-HBAMA-*b*-DMAEMA)-*b*-P(Lys) (P) polymer through multistep polymerization methods and all synthesis steps and characterization methods of the polymers were detailed in the Supporting Information. The multimodal core/shell AuNRd@P-DOX/ICG/ISIS5132 hybrid nanoparticles were fabricated in three steps. First was the conjugation of the amphiphilic polycationic P-DOX polymer with AuNRd, followed by the encapsulation of ICG molecules into AuNRd@P-DOX nanoparticles, and finally followed by the binding of antisense oligonucleotide (ISIS5132) on the surface of AuNRd@P-DOX/ICG particles (Scheme 1). The fructosylated sugar shell of the hybrid particles provides a great potential in targeting breast cancer cells and therefore improving nanoparticle accumulation at the tumor site by targeting GLUT5.[4,27] As shown in the schematic synthesis route of the tetrablock copolymer, first, DOX-conjugated cationic glycopeptide tetrablock polymer (P(FrucMA-*b*-HBAMA-*b*-DMAEMA)-*b*-P(Lys)-DOX), (P-DOX), was initially prepared through ROP and RAFT polymerization techniques with the combination of click reaction (Scheme S1). The characterization of P(FrucMA-*b*-HBAMA-*b*-DMAEMA)-*b*-P(Lys) tetrablock copolymer and its precursors is discussed in Figures S1−S7. The molecular weight and structure of the tetrablock copolymer were defined by GPC and ^{1}H-NMR (Table S1, Figures S3 and S5). The number average molecular weight (M_n) of the tetrablock copolymer was found to be 13.7 kDa (PDI = 1.27) via GPC analysis. After DOX conjugation, the reduction of the peak intensity at 9.75 ppm and the appearance of two OH peaks of DOX at 13.26 ppm and at 14.03 ppm in the ^{1}H-NMR spectrum confirmed that DOX was successfully conjugated on aldehyde groups of polymer backbone through pH-sensitive cleavable imine bonds (Figure S3). DOX conjugation efficiency was determined to be 83% in the ^{1}H-NMR spectrum regarding the peak integration ratios at 14.03 and 9.75 ppm. The AuNRd were functionalized with DOX-conjugated tetrablock polymer to obtain AuNRd@P-DOX nanoparticles based on the formation of the unique bonding between AuNRd and thiol groups of the polymer. After that, ICG molecules were encapsulated into AuNRd@P-DOX to provide photodynamic therapy in addition to chemo-/photothermal therapy. Although ICG is a well-studied photosensitizer, which can generate singlet oxygen species under 808 nm NIR irradiation, it has some intrinsic limitations such as poor solubility, instability, concentration-dependent aggregation, and rapid clearance.[21] These restrictions result in low therapeutic efficiency. To overcome these drawbacks, as mentioned earlier, the construction of an appropriate drug carrier to load ICG is of great necessity.[21] To overcome these undesired limits of ICG, the AuNRd@P-DOX was incubated in an aqueous suspension of ICG for encapsulation. As a result of that, AuNRd@P-DOX/ICG nanoparticles with the desired chemotherapeutic, photothermal and photodynamic properties were produced. The TEM images of AuNRd@P-DOX/ICG nanoparticles were given in Figure 1C, in which the polymer layer can be observed clearly on the surface of AuNRd. The thickness of the polymer layer was determined to be ∼106 nm from the TEM image.

In our design, to enhance the selective apoptosis of breast cancer cells, we also decorated the AuNRd@P-DOX/ICG particles with antisense-ISIS5132 to obtain AuNRd@P-DOX/ICG/ISIS5132 hybrid nanoparticles. The zeta potential values for AuNRd after polymer coating and ISIS5132 conjugation are given in Figure 1G. As can be seen, the zeta potential (ζ) values for AuNRd after polymer coating and ISIS5132 conjugation were changed dramatically, as expected. Before the coating of P-DOX, the zeta potential of AuNRd was about +50.1 ± 1.10 mV because of the presence of CTAB on the surface of AuNRd, which is important for the stabilization of the particles.[28] Afterward, covering the cationic glycopeptide tetrablock polymer, the ζ potential of the AuNRd@P-DOX/ICG was measured as +37.5 ± 1.09 mV (Figure 1G). It is well known that antisense ISIS5132 has a high affinity to down-regulate c-Raf expression and it makes ISIS5132 a unique molecular ligand for targeted cancer therapy.[29] Positively charged glycopeptide tetrablock polymer on the surface of AuNRd can create an electrostatic adsorption area with negatively charged ISIS5132. In this direction, AuNRd@P-DOX/ICG/ISIS5132 was prepared by mixing ISIS5132 and the AuNRd@P-DOX/ICG specified at a predetermined N/P ratio (ratio of nitrogen groups (N) on polymers to phosphate (P) of ISIS5132) in water solution for 1 h at room temperature. To find the optimum ratio for the best stabilizing the ISIS5132, a series of AuNRd@P-DOX/ICG/ISIS5132 conjugates were formed at various N/P ratios (0.5/1, 1/1, 2/1). According to the inserted image in Figure 1F, the electrophoresis mobility shift assay indicated that the maximum degree was observed at a N/P ratio of 2 and no optical differences were monitored at higher N/P ratios. After the ISIS5132 conjugated on the AuNRd@P-DOX/ICG nanoparticles, the zeta potential value declined and measured as −7.39 ± 0.16 mV, indicating the successful immobilization of ISIS5132 on AuNRd.[19]

The AuNRd@P-DOX/ICG nanoparticles and all components of the particles were characterized by UV−vis measurement, as seen in Figure 1D. The AuNRd have two typical adsorption bands, a weak transverse surface plasmon resonance wavelength at approximately 520 nm and a strong longitudinal surface plasmon resonance wavelength at approximately 833 nm (Figure 1D). After DOX-conjugated polymer coating, the specific absorbance of DOX was observed at 488 nm, which indicates the coating of DOX-conjugated polymer on AuNRd. After ICG loading, the new absorbance appeared at around 400 nm as the same as the UV−vis spectrum of ICG as a proof of ICG encapsulation. The ICG encapsulation efficiency was determined as 64.06% using the measurement of the absorption at 795 nm.[30] The chemical composition of the AuNRd@P-DOX/ICG nanoparticles and their precursors was identified by ATR-FTIR analysis (Figure 1E and Figure S4). In the ATR-FTIR spectrum of CTAB-AuNRd, the absorption peaks were observed at 2920−2840 cm^{-1}, corresponding to the C−H stretch of the hydrophobic alkyl chain layers of CTAB.[31] Moreover, the specific absorption band of the asymmetric bending $N^+-(CH_3)_3$ appeared at 1466 cm^{-1} as a proof of the presence of CTAB on AuNRd.[19,31] After DOX-conjugated glycopeptide polymer coating was applied to AuNRd, the characteristic peaks of DOX were observed at 1623 and 1583 cm^{-1} and the major characteristic peaks of glycopeptide polymer were also presented in the ATR-FTIR spectrum of AuNRd@P-DOX. The specific C−H stretch bands of polymer appeared at 2800−2900 cm^{-1}, while the C−O bands were observed between 1050 and 1100 cm^{-1}. The −COH band corresponding to the aldehyde structure in the HBAMA group is seen at 1693 cm^{-1}. The specific (C−H(−N(CH$_3$)$_2$))

https://doi.org/10.1021/acsami.2c21180
ACS Appl. Mater. Interfaces 2023, 15, 9080−9098

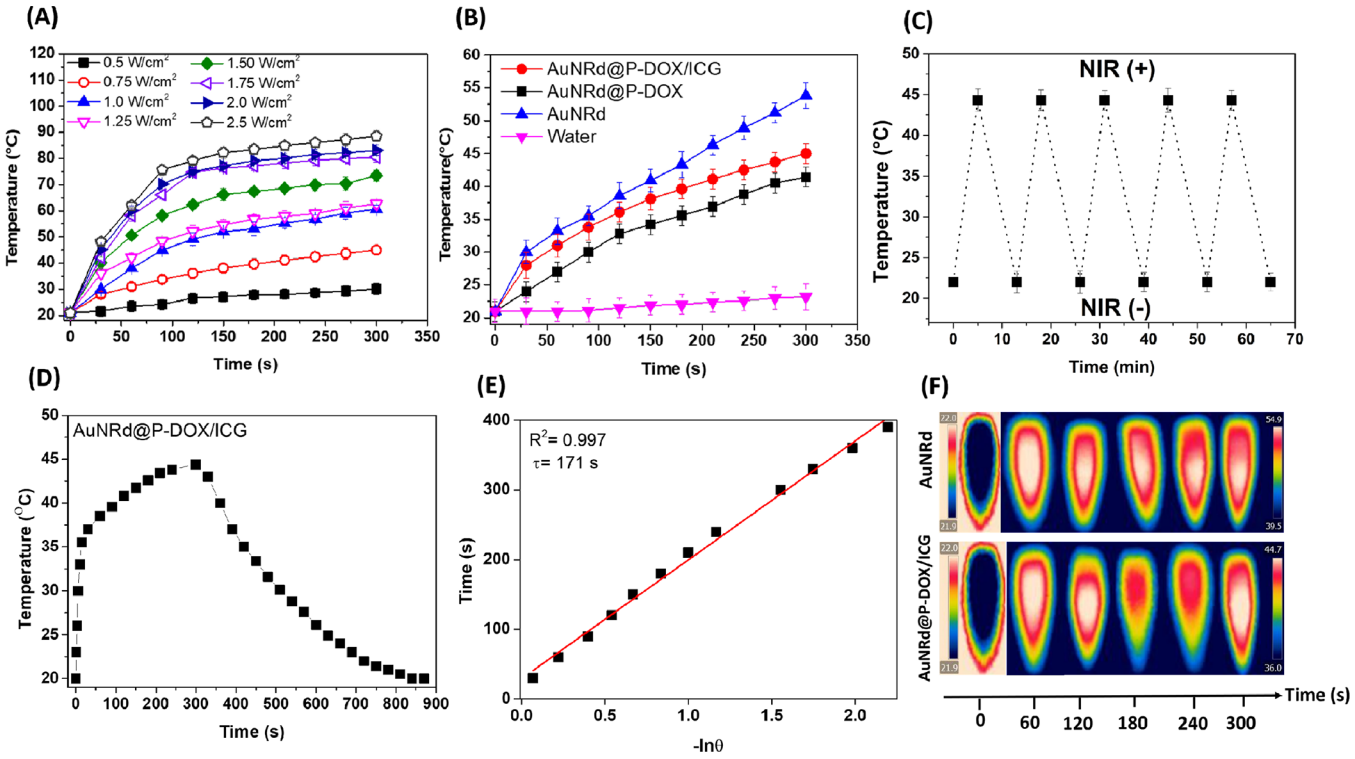

Figure 2. Photothermal efficiency of (A) the AuNRd@P-DOX/ICG (62.50 μg/mL) aqueous solution under 808 nm laser irradiation at different laser intensities for 300 s, (B) AuNRd, AuNRd@P-DOX, AuNRd@P-DOX/ICG, and water under 808 nm NIR (0.75 W/cm^2) for 300 s; (C) photothermal stability of AuNRd@P-DOX/ICG (62.50 μg/mL) over five cycles of repeated laser irradiation; (D) photothermal efficiency of the AuNRd@P-DOX/ICG (62.50 μg/mL) under 808 nm NIR (0.75 W/cm^2) for 300 s and then allowing to cool to room temperature under a natural cooling process after shutting off the laser; (E) the linear regression between the cooling period and negative natural logarithm of driving force temperature of AuNRd@P-DOX/ICG (62.50 μg/mL); and (F) thermal images of AuNRd and AuNRd@P-DOX/ICG solutions under the irradiation by 808 nm laser (0.75 W/cm ^{2}) for 300 s.

stretching vibration bands of the DMAEMA groups appeared at 2770−2940 cm^{-1}. After ICG loading, the similar peak shifts were observed with the polymer so we could not confirm the ICG encapsulation by ATR-FTIR analysis. As a result, it can be said that the AuNRd@P-DOX/ICG/ISIS5132 nanoparticles were successfully fabricated.

pH-sensitive DOX Release Behavior of Phototherapeutic Nanoparticles. First, we investigated the chemotherapy efficiency of the hybrid nanoparticles. The acid-cleavable imine bonding synthesized DOX-conjugated glycopeptide polymer between DOX and polymer to obtain pH-triggered DOX release. The pH-depended DOX release of the particles was studied at different pH media at 37 °C. The DOX release profiles of P-DOX and AuNRd@P-DOX were performed at pH 5.5, 6.8, and 7.4, resembling the pH values of tumor microenvironment and healthy tissue conditions. We compared the DOX release profiles between P-DOX polymer and AuNRd@P-DOX nanoparticles in the same conditions (Figure S6). Both P-DOX and AuNRd@P-DOX nanoparticles showed similar DOX-release behavior. The amount of released DOX from AuNRd@P-DOX nanoparticles was significantly increased from 10 to 80% at pH 7.4 and pH = 5.5 within 72 h, respectively. The difference in the pH-dependent release behavior of particles was confirmed that DOX released rapidly by cleavage of acid-labile imine bonds of the polymer as desired. As a result, it was found that the release amount of DOX was much higher in acidic conditions, which is important for cancer treatment since cancerous tissues are more acidic than healthy tissues.[32]

***In Vitro* Photothermal Conversion Efficiency.** As mentioned above, the optical properties of AuNRd@P-DOX/ICG solution (62.50 μg/mL) were investigated using a UV−vis spectrophotometer (Figure 1D) and a strong absorption in the NIR region (700−900 nm) was observed. This absorption in the NIR region plays an important role in the NIR-induced photothermal effect of the particles for cancer therapy. This absorption is the major sign of the photothermal conversion ability of the particles in the NIR region. Herein, under NIR irradiation, the expectation from phototherapeutic nanoparticles expects to reach a hyperthermic temperature (40−45 °C) to kill cancer cells with the lowest and most effective laser intensity and irradiation time within the tolerance of skin burning thresholds. This is of course important for *in vivo* applications. In this context, it can be said that the power of the laser is a major point and the usage of the high laser power (1−48 W/cm^2) is reported to be unsuitable for clinical treatments.[33] Therefore, it can be said that a desirable laser power would be below 1 W/cm^2 for clinical trials. Starting from this point, first, we investigate the photothermal conversion efficiency of the nanoparticles. For this purpose, AuNRd@P-DOX/ICG/ISIS5132 (62.50 μg/mL) was exposed to the 808 nm laser at different power settings of 0.5, 0.75, 1, 1.25, 1.50, 1.75, 2.0, and 2.5 W/cm^2 for 300 s to obtain the photothermal heating curves of the particles (Figure 2A). The temperature of the AuNRd@P-DOX/ICG/ISIS5132 solution increased from 30.1 to 88.5 °C after laser irradiation at 0.50 and 2.5 W/cm^2 for 300 s, respectively. It was expected result that the temperature of the

https://doi.org/10.1021/acsami.2c21180
ACS Appl. Mater. Interfaces 2023, 15, 9080−9098

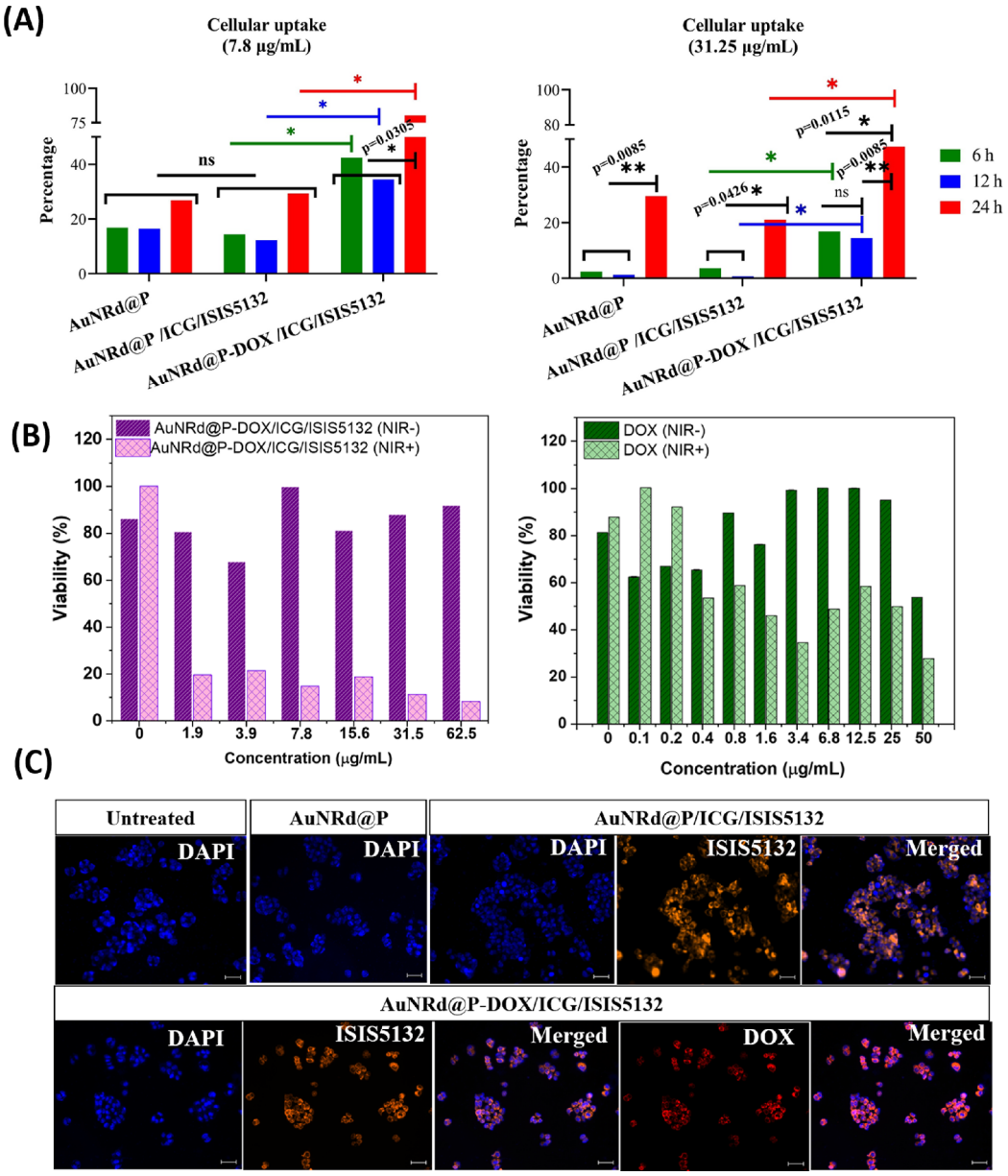

Figure 3. (A) Flow cytometric uptake analysis of MCF7 cells. Uptake was performed accordingly at the 6th, 12th, and 24th hours with the indicated concentrations of the nanoparticles (31.25 and 7.8 μg/mL) including AuNRd@P, AuNRd@P/ICG/ISIS5132, and AuNRd@P-DOX/ICG/ISIS5132, and as a control, DOX was used. The uptake analysis between time intervals, particularly for the 6th and 12th, and concentration showed a negative correlation for nanoparticles. *p < 0.05, **p < 0.01, ***p < 0.001. (B) Viability results from MTT experiment for DOX and AuNRd@P-DOX/ICG/ISIS5132 with/without NIR exposure after 24 h of treatment. NIR exposure was performed at the 6th hour of treatment. (C) MCF7 cells were visualized for uptake control after 12 h of treatment with AuNRd@P, AuNRd@P/ICG/ISIS5132, and AuNRd@P-DOX/ICG/ISIS5132 nanoparticles at the 3.9 μg/mL concentration. Nucleus stained with DAPI (blue), nanoparticles that contain ISIS5132 oligonucleotide (conjugated with Cyanine-3 (Cy3)) and DOX were pseudocolored in yellow and red, respectively. Scale bar = 50 μm, DOX: doxorubicin.

particles solution would increase with the increasing laser intensity and the irradiation time. The temperature of AuNRd@P-DOX/ICG/ISIS5132 solution reached 45 °C under 0.75 W/cm^2 808 nm NIR irradiation. This significant result illustrates that the AuNRd@P-DOX/ICG/ISIS5132 is suitable for use as a photothermal agent in clinical trials.

The photothermal conversion efficiency of the AuNRd@P-DOX/ICG particles was tested against its constituent components (AuNRd and AuNRd@P-DOX) and against DIW as a control group (Figure 2B). It is observed that, while DIW temperature slightly increased from 21 to 23.2 °C, the temperature of AuNRd@P-DOX/ICG increased dramatically, from 21 to 45 °C, under the same conditions. The thermal images of AuNRd@P-DOX/ICG are given in Figure 2F. This result indicated that AuNRd@P-DOX/ICG particles are a good candidate for use as a photothermal therapeutic agent due to their light harvesting and heat conversion ability. It is an expected result that AuNRd exhibited more temperature change than both AuNRd@P-DOX and AuNRd@P-DOX/ICG. As seen in the thermal images of AuNRd, temperature changes are higher than AuNRd@P-DOX/ICG depending on irradiation time (Figure 2F). The

https://doi.org/10.1021/acsami.2c21180
ACS Appl. Mater. Interfaces 2023, 15, 9080−9098

maximum temperature values were recorded as 53.8, 43.8, and 45 °C for AuNRd, AuNRd@P-DOX, and AuNRd@P-DOX/ICG under 0.75 W/cm^2 808 nm NIR irradiation within 300 s, respectively. The change in photothermal performance can explain that these temperature changes can be explained by the change of photothermal performance by surface modification of AuNRd.[31] On the other hand, a remarkable difference in temperature changes between AuNRd@P-DOX and AuNRd@P-DOX/ICG was observed. This may be explained by the presence of ICG, which can act as a photothermal agent and produce singlet oxygen derivatives in the NIR region.[34]

The photothermal stability of a photothermal therapy agent is an important parameter to consider to reveal its reusability performance. To obtain an efficient photothermal effect from the system, the photothermal therapy agent can be reached at the same temperature values for each NIR irradiation cycle. As seen in Figure 2C, to investigate the photothermal stability, AuNRd@P-DOX/ICG was irradiated by 808 nm NIR (0.75 W/cm^2) for 300 s and turning off the laser for 480 s to cool down to the initial temperature. These procedures were repeated five times. It was observed that AuNRd@P-DOX/ICG exhibited excellent photothermal stability under laser irradiation, reaching almost the same temperature for each irradiation cycle.

The photothermal conversion efficiency (η) plays a crucial role in photothermal therapy. In this context, we determined the photothermal conversion efficiency of AuNRd@P-DOX/ICG following a previous method.[35,36] AuNRd@P-DOX/ICG (62.50 μg/mL) was first exposed to the 808 nm NIR laser (0.75 W/cm^2) for 300 s; after which, the laser was turned off, and the solution was allowed to cool to ambient temperature under a natural cooling process (Figure 2D). The linear time data versus $-\ln(\theta)$ obtained from the cooling period of phototherapeutic nanoparticle was given in Figure 2E, and τs was determined to be 171 s. According to eq 1, the 808 nm laser heat conversion efficiency (η) of the AuNRd@P-DOX/ICG was determined to be 57.7%. As previously reported, gold-based PTT agents showed lower heat conversion efficiency than we obtained.[35] This is an expected result because in our nanocarrier system; we also used ICG as both PDT and PTT agents. As seen in our photothermal conversion results (Figure 2B), ICG-loaded nanoparticles exhibited more temperature increase and also high η value as seen in similar previous works.[37] Therefore, our hybrid nanocarriers system exhibited an efficient and high photothermal conversion efficiency value.

Cellular Uptake of Phototherapeutic Nanoparticles. For *in vitro* evaluations, we first demonstrated all nanoparticles including AuNRd@P, AuNRd@P/ICG/ISIS5132, and AuNRd@P-DOX/ICG/ISIS5132 could be taken up by MCF7 cells. We observed the outcome at the 6th, 12th, and 24th hours of treatment following DOX signal and/or Cy3-conjugated ISIS5132 oligonucleotide by flow cytometry. Free DOX was used as a positive control in this experiment. MCF7 cells were treated with 31.25 and 7.8 μg/mL nanoparticle concentration (Figure 3A) and healthy control CCD-1079Sk cells treated with 7.8 μg/mL for all groups and as a positive control, free DOX groups were compared. Raw uptake changes of all nanoparticles and free DOX with three-time intervals and two different concentrations are provided in Figure S8. The results showed that, without DOX, the nanoparticle uptake was limited and required treatment with higher concentrations or longer treatment durations. For example, treatment with AuNRd@P at 31.25 μg/mL concentration showed increased uptake capacity, while higher concentration and longer cultivation occurred over time intervals (p = 0.0085). However, CCD-1079Sk cells did show significant uptake for nanoparticles, except for free DOX (Figure S8C). Moreover, the cellular internalization of AuNRd@P-DOX/ICG/ISIS5132 for MCF-7 cells (GLUT5 over-expressing) was more efficient than CDD-1079Sk cells, showing the specific interaction between fructose and GLUT5. Additionally, AuNRd@P/ICG/ISIS5132 presented a similar uptake behavior (p = 0.0426) at 31.25 μg/mL treatment concentration for MCF7 cells. By contrast, if DOX is included in the nanoparticle system, the uptake becomes more facilitated only for MCF7 cells particularly for AuNRd@P-DOX/ICG/ISIS5132 even with a 4-fold diluted concentration administered, and through longer cultivation, the uptake increases significantly (p = 0.0305 for 7.8 μg/mL concentration when compared over between time intervals, and p = 0.0349 when compared the DOX-free version; in Figure 3A). Increased modulation of the uptake when DOX is incorporated in the nanoparticle system shifts the cellular interaction prominently. Shen et al. studied the DOX net uptake and cytoplasmic efflux on multidrug resistant breast cancer cells and compared the outcome with wild-type. Numerous studies have shown that DOX intercalates into DNA and subsequently inhibits DNA polymerase and nucleic acid synthesis.[38] For MCF7 cells in this study, the uptake observation showed that the presence of DOX facilitated the AuNRd@P-DOX/ICG/ISIS5132 uptake. Based on that, we assumed the role of DOX in the nanoparticle system explains, at least in part, the apparent increase of DOX-carrying versions of nanoparticles' net uptake in the MCF7 cells contingent.

In addition, we also performed ICP-MS measurement to determine the internal particle concentrations (7.8 μg/mL) within the MCF7 cell line. The internal gold concentration was determined as 4.01, 10.15, and 10.30 ng/mL for 6, 12 and 24 h incubations, respectively. The internal gold nanoparticle concentration in cell culture increased with increasing incubation time that is compatible with the flow cytometry results.

***In Vitro* Dark- and Photo-cytotoxicity of Phototherapeutic Nanoparticles.** We proceeded to determine the working concentration while dark- or with NIR-induced cytotoxicity for further experiments. All nanoparticle groups were treated with 10 different serially diluted concentrations for 24 and 48 h. The viability changes showed a concentration and/or time-dependent decrease when higher concentrations were administered (Figure 3B). Time interval dependent viability changes from dark-cytotoxicity evaluations are presented in Figure S9. The healthy control group CCD-1079Sk cells did not presented any significant changes with or without NIR exposure, which is positively correlated with the uptake outcome. The free DOX has more disrupting effect than all the nanoparticle groups (Figure S9C). Furthermore, the half-maximal inhibitory concentration values (IC_{50}) were determined for MCF7 cells (Table S2). For the phototherapeutic nanoparticles (AuNRd@P-DOX/ICG/ISIS5132), the IC_{50} value was 2.557 μg/mL and following NIR exposure the IC_{50} value magnified to 311.338 μg/mL. This result demonstrated that phototherapeutic nanoparticles exhibit the desired synergic triple effect and reduce viability, which is known as a critical tumor treatment modality. Notably, potential interference with MTT reagent and DOX was

https://doi.org/10.1021/acsami.2c21180
ACS Appl. Mater. Interfaces 2023, 15, 9080−9098

eliminated by different studies.[39] However, to observe the precise outcome, ISIS5132 was conjugated with Cy3. The Cy3 (ex:548−552/em:562−570 nm) and DOX (ex:595/em:470 nm) have close excitation and emission range in the fluorescent spectrum. Additionally, MTT is quantified by measuring a change in absorbance (560 nm excitation/590 nm emission) when all three are considered together; closeness in the spectrum can cause a significant increase in the IC_{50} level. Hence, the significant increase for the IC_{50} level negatively correlated with reduced viability. Along with this, an application of 3.9 μg/mL (which was the closest concentration to the IC_{50} value range of AuNRd@P-DOX/ICG/ISIS5132) and 4-fold and 8-fold diluted concentrations (0.97 and 0.24 μg/mL) were employed for further experiments. Then, we examined the ability of this selected concentration (3.9 μg/mL) over time by fluorescence microscopy and visualized them for uptake control after 12 h of treatment with AuNRd@P, AuNRd@P/ICG/ISIS5132, and AuNRd@P-DOX/ICG/ISIS5132 (Figure 3C). In addition, the raw microscope images of all concentrations from the uptake process were compiled in Figure S10. During these experiments, the ISIS5132 oligonucleotide was conjugated with the Cy3-label to determine the nanoparticle localization intracellularly where a DOX signal cannot be detected due to the low concentrations inside the nanoparticle system.

Notably, the Cy3-label and DOX have close excitation and emission ranges in the fluorescent spectrum. They are the main reason for performing imaging for the uptake by the selected concentrations, even if the flow cytometry quantifies it.

Microscopy images confirmed that the phototherapeutic nanoparticles were uptake and fully localized in the cytoplasmic areas of the MCF7 cells at the 12th hour. Nuclei staining provided viable cell clusters after treatments, and intracellularly Cy3/DOX signals were observed. Interestingly, AuNRd@P/ICG/ISIS5132 groups showed free nanoparticles outside of the cells (shown as bold yellow spots in Figure 3C, upper right image). In contrast to this group's flow cytometric uptake results, the reduced concentration increased the cellular uptake. Nevertheless, when the nanoparticles were combined with DOX, the uptake capacity expanded inversely to the concentration.

WOUND HEALING

After that, we focused on cell migration changes during treatments and NIR exposure on MCF7 cells via wound healing assay. As is known, wound closure dynamics differ between cell lines.[40] In this study, the wound closure pattern was nonlinear almost for all groups (Figure S11A,B). Obtaining quantitative data about cell motility usually requires a lot of images, visualization equipment, and software[41] and mainly provides semiquantitative results.[42] Hence, we employed a different approach to evaluating wound closure dynamics through time and aimed to provide treatment outcomes as precisely as possible. To evaluate proliferation status and precise wound closure capacity after treatment and NIR exposure, analyses were performed by using the ImageJ[43] via the cell counter option inside the scratch areas, and the cell quantity was determined as described previously.[25] Both raw images and analysis of all groups with/without NIR exposure are outlined and compiled in Figure S11C. The wound scratches were observed for untreated, DOX, AuNRd@P, AuNRd@P/ICG/ISIS5132, and AuNRd@P-DOX/ICG/ISIS5132, and carried DOX groups with/without NIR irradiation. The concentration of DOX was 4.042 μg/mL (IC_{50}), and carried DOX concentrations were; 0.084 μg/mL for 3.9 and 0.022 μg/mL for 0.97 μg/mL nanoparticle concentrations, respectively. Over time, cell migration was observed mainly in the untreated group as expected, whereas free DOX treatment does not. Our comprehensive examination of the healing status of the wound area by nanoparticles showed that concentration or time-dependent inhibition occurs when compared with untreated wounds. We observed that wound closure in the AuNRd@P-DOX/ICG/ISIS5132 showed no migration through the wound area even without NIR exposure. Additionally, the treatment with two different concentrations did not affect the cell proliferation outside of the scratches. Over time, treatments with other nanoparticle groups showed a decreased closure speed depending on the concentration, while areas outside of the scratch areas also exhibited different cell proliferation rates (Figure 4).

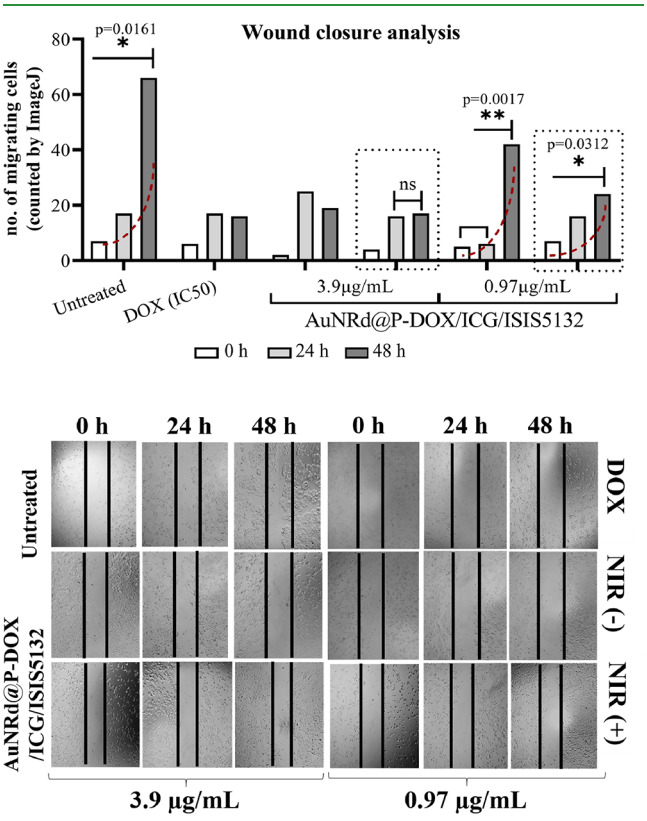

Figure 4. Graphs show the quantification of the migrated cells into the wound area. Through time, wound closure shows that only untreated cells could close the area, while the scratch area was closing slowly in the presence of AuNRd@P, AuNRd@P/ICG/ISIS5132, and carried DOX for both of the concentrations and with NIR exposure as well. In the AuNRd@P-DOX/ICG/ISIS5132 treatment group, wound closure was not fully observed through time and NIR exposure. The red and black dashed lines indicate the increased migrating cell amount and NIR exposed groups, respectively. The data were expressed as the mean ± SD. *$p < 0.05$, **$p < 0.01$, ns: not significant. The lower panel shows representative wound healing microphotographs. Evaluation of cell migration at 0 h (beginning), 24 h, and 48 h after treatment with nanoparticles and as a control DOX (IC_{50} value 4.042 μg/mL) treatment on MCF7 cells is shown. The light microscope images were acquired using a microscope lens adapter for smartphones, and each scale coordinates were used for microscope centering for each time interval/group—magnification 10×.

https://doi.org/10.1021/acsami.2c21180
ACS Appl. Mater. Interfaces 2023, 15, 9080−9098

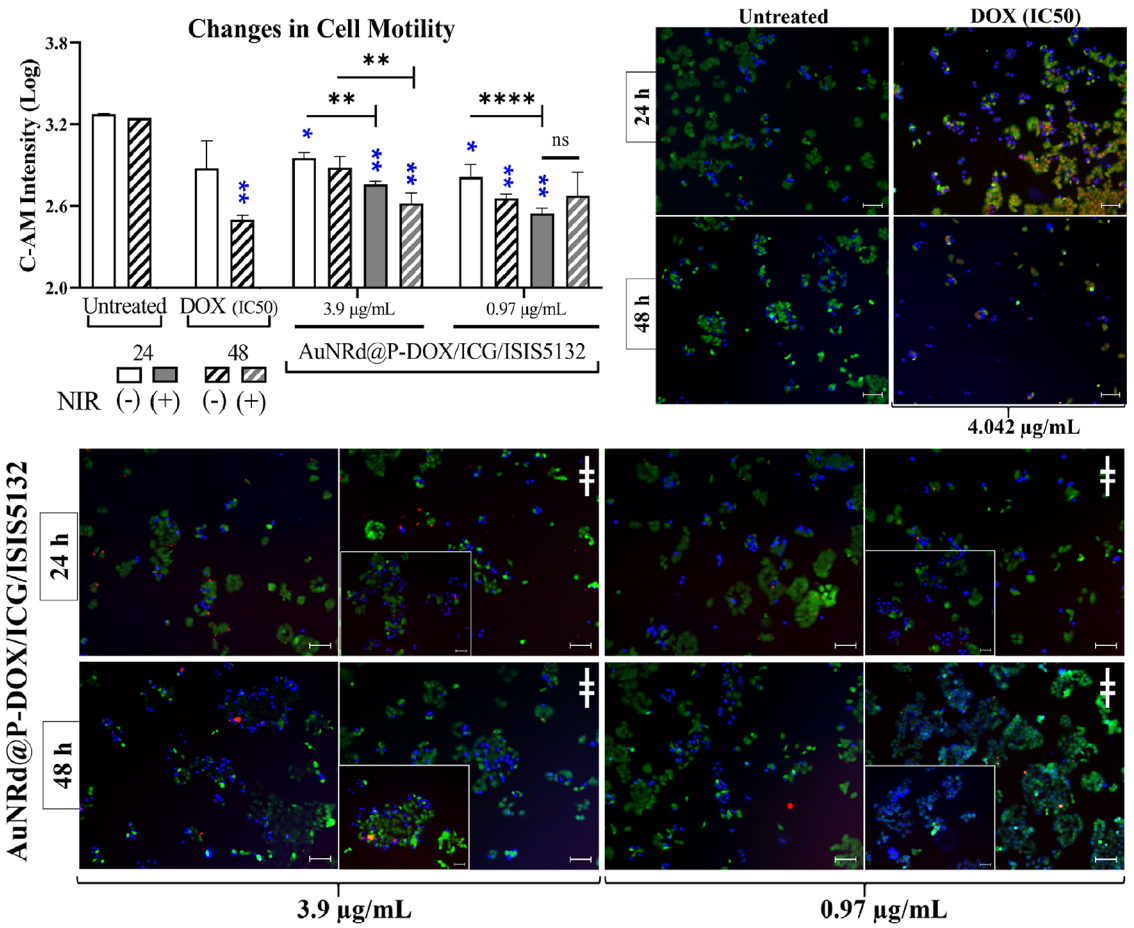

Figure 5. Graph shows changes in cell motility after treatment with DOX (IC_{50}; 4.042 μg/mL) and AuNRd@P-DOX/ICG/ISIS5132 with/without NIR exposure. All of the blue stars indicate comparisons of the untreated versus groups per time interval. *p < 0.05, **p < 0.01, ****p < 0.0001. Microphotographs of MCF7 cells stained with calcein-AM. Cultivations were stained for 2 h with 0.2 mM calcein-AM and then washed before visualization. Images show cells in different concentrations of AuNRd@P-DOX/ICG/ISIS5132 (3.9 and 0.97 μg/mL, respectively) with/without NIR exposure. Merged images include calcein-AM (green), the DOX or Cy5-tagged-ISIS5132 oligonucleotide (red), and nuclei (blue). "alveolar click sign" indicates NIR exposure. Magnification 10× and insets 20×. Scale bar = 50 μm. DOX: doxorubicin.

IN VITRO PHOTOTHERMAL AND PHOTODYNAMIC THERAPY

Fluorescent probes such as ester derivatives like calcein-AM have become a valuable tool for determining cellular health, adhesion,[44] proliferation, motility,[45] and changes in intracellular pH,[46] etc. In addition to its simplicity, the utility of calcein-AM staining in this study after the treatment with nanoparticles both with and without NIR irradiation was demonstrated. We continued analyzing the effect through cellular treatments based on cell morphology/adherence capability. For continued follow-up during treatments or the cultivation process, visualization of the cell morphology is a vital tool.[47] This may easily be demonstrated, especially by detecting cell changes with fluorescent dyes. Observation of the calcein-AM, which acts upon cellular esterases, indicated that most of the MCF7 cells remained viable, morphologically normal, and well distributed for the untreated group over time. Similar results were observed for the AuNRd@P, and AuNRd@P/ICG/ISIS5132 groups. Stain intensity was generally strong but varied among treatment groups, especially those without NIR exposure and free DOX groups (Figure 5).

Detailed morphological features of untreated, DOX (IC_{50}), AuNRd@P, AuNRd@P/ICG/ISIS5132, AuNRd@P-DOX/ICG/ISIS5132 and carried DOX concentrations are presented in Figure S12. The free DOX treatment exhibited a significant decrease in cell adherence capability and vitality when compared to the untreated group at 48 h (p = 0.0021). AuNRd@P-DOX/ICG/ISIS5132 showed a significant reduction in the intensity value when compared with an untreated group through concentration and over time (at 3.9 μg/mL concentration p = 0.0134 for 24 h without NIR exposure; p = 0.0018 and p = 0.0014 for 48 h with NIR exposure, respectively; at 0.97 μg/mL concentration p = 0.0385 and p = 0.0031 for 24 and 48 h sequentially without NIR exposure as well as p = 0.0027 for 48 h with NIR exposure). Distributively, the nanoparticles showed a decreased cellular motility pattern, particularly after NIR exposure, which was the expected positive correlation over time (when compared with/without NIR exposure at 3.9 μg/mL concentration p = 0.0015 and p = 0.0053 for 24 and 48 h of treatment, respectively. p < 0.0001 at 0.97 μg/mL concentration for 24 h of treatment). The data suggest that the loss of NIR-induced adherence capability significantly altered the outcome in a dose-dependent manner for MCF7 cells. Staining with calcium binding-calcein dye showed the nanoparticle treatment's effects on adherence capability and vitality simultaneously. In particular, the AuNRd@P-DOX/ICG/ISIS5132 exhibited a decreased profile for the MCF7 cells. The concentration difference of particles

https://doi.org/10.1021/acsami.2c21180
ACS Appl. Mater. Interfaces 2023, 15, 9080−9098

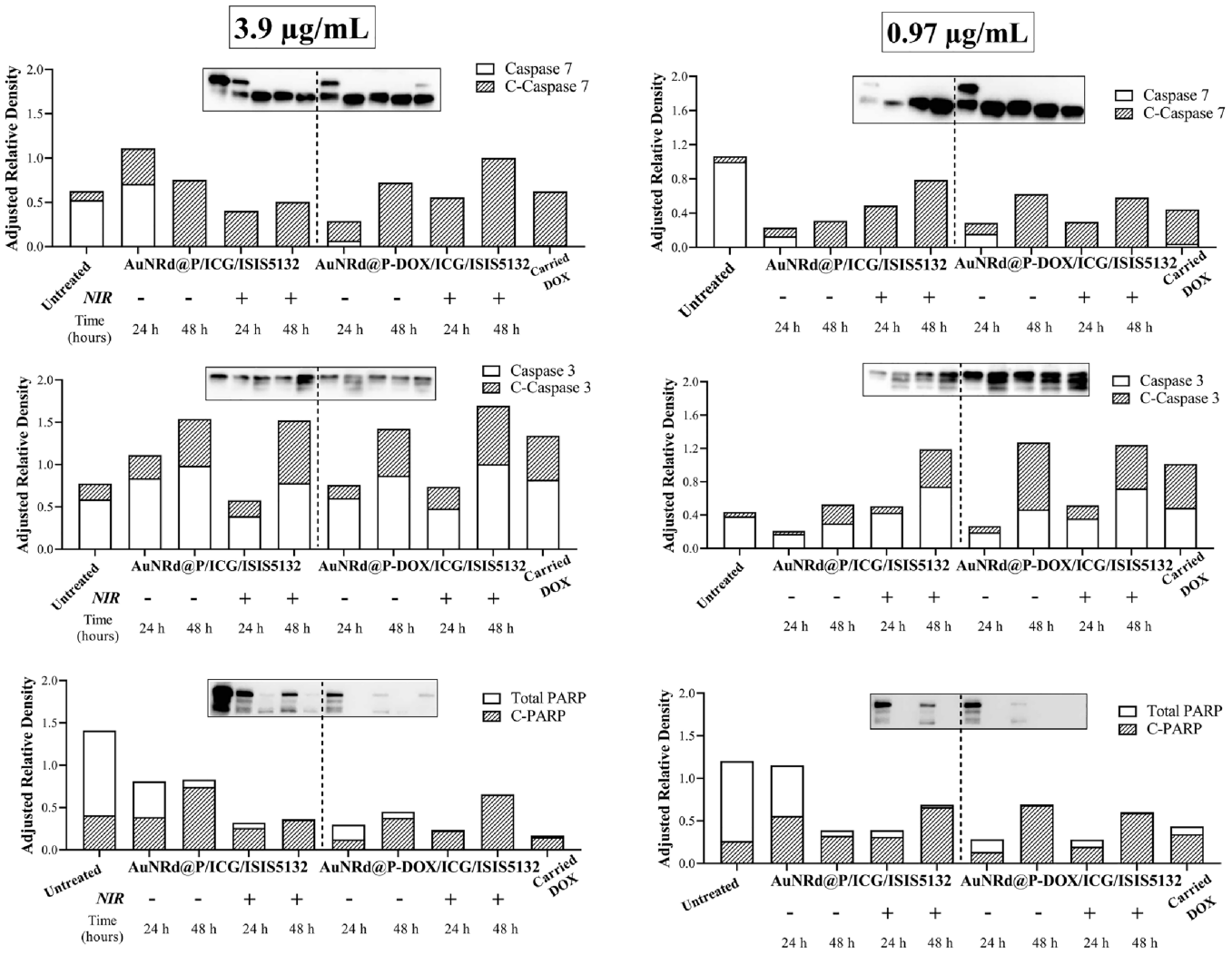

Figure 6. Western blot results of caspase-7, caspase-3, PARP, and cleaved products after 24 and 48 h treatment with the indicated concentrations of the nanoparticles including untreated, AuNRd@P/ICG/ISIS5132, AuNRd@P-DOX/ICG/ISIS5132, and carried DOX with/without NIR exposure. h: hour. DOX: doxorubicin.

also affects the magnitude of the changes. Alternatively, along with calcein-AM, we used another fluorescence to track nanoparticles by conjugating ISIS5132 with Cy5. Dual fluorescence tracking minimized the aberrations with the imaging and increased the rendering.

Moreover, apoptotic outcomes were determined to investigate the mechanisms underlying the cell death process in MCF7 cells. As is known, many proteins are cleaved by caspases during apoptosis.[48] After our wound healing and cell motility observations, we directly aimed to show whether apoptosis occurs in the desired way without necrosis. We evaluated this in the most accurate direction via harnessing apoptotic protein expressions, ROS production, and confirmed via apoptotic cell profile changes. In addition, we wanted to determine the most effective concentration of AuNRd@P-DOX/ICG/ISIS5132 treatment.

Semiquantification of protein expression changes by western blotting is the most commonly used molecular biology technique.[49] However, during comparative analyses, researchers use normalization controls to provide critical outcomes.[49] We preferred two separate normalization controls, in this study including GAPDH and β-actin. We then examined the most stable normalization variable by using the BestKeeper interface[50] before determining relative expression changes between variables. Of the two, β-actin presented a more stable pattern than GAPDH (Pearson correlation coefficient $r = 0.837$ and $p = 0.025$), considering all of the nanoparticle treatments and NIR exposure (Figure S13).

Specifically, changes in total and cleaved protein products of caspase-7, caspase-3, and poly-ADP Ribose (PARP) relative protein expressions (relative to the β-actin) were determined by comparing time intervals, concentrations, and the presence or absence of NIR irradiation (Figure 6). Outcomes were compared with the untreated, free DOX, and nanoparticle systems carrying DOX at different concentrations. The triple actions of the AuNRd@P-DOX/ICG/ISIS5132 and its DOX-free version AuNRd@P/ICG/ISIS5132 were cultured up to 24 and 48 h for the two selected concentrations including 3.9 and 0.97 μg/mL. At the 6th hour of cultivation, NIR irradiation was performed for both groups and the outcome was evaluated in terms of all variables starting with western blotting. Thus, concentration-dependent apoptotic protein behavior was evaluated in detail. At 3.9 μg/mL concentration treatment, the changes in the cellular expression and cleavage of the caspase-7 were found to be significant over time and between groups ($p = 0.0013$). Caspase-7 was cleaved by treatments and

https://doi.org/10.1021/acsami.2c21180
ACS Appl. Mater. Interfaces 2023, 15, 9080−9098

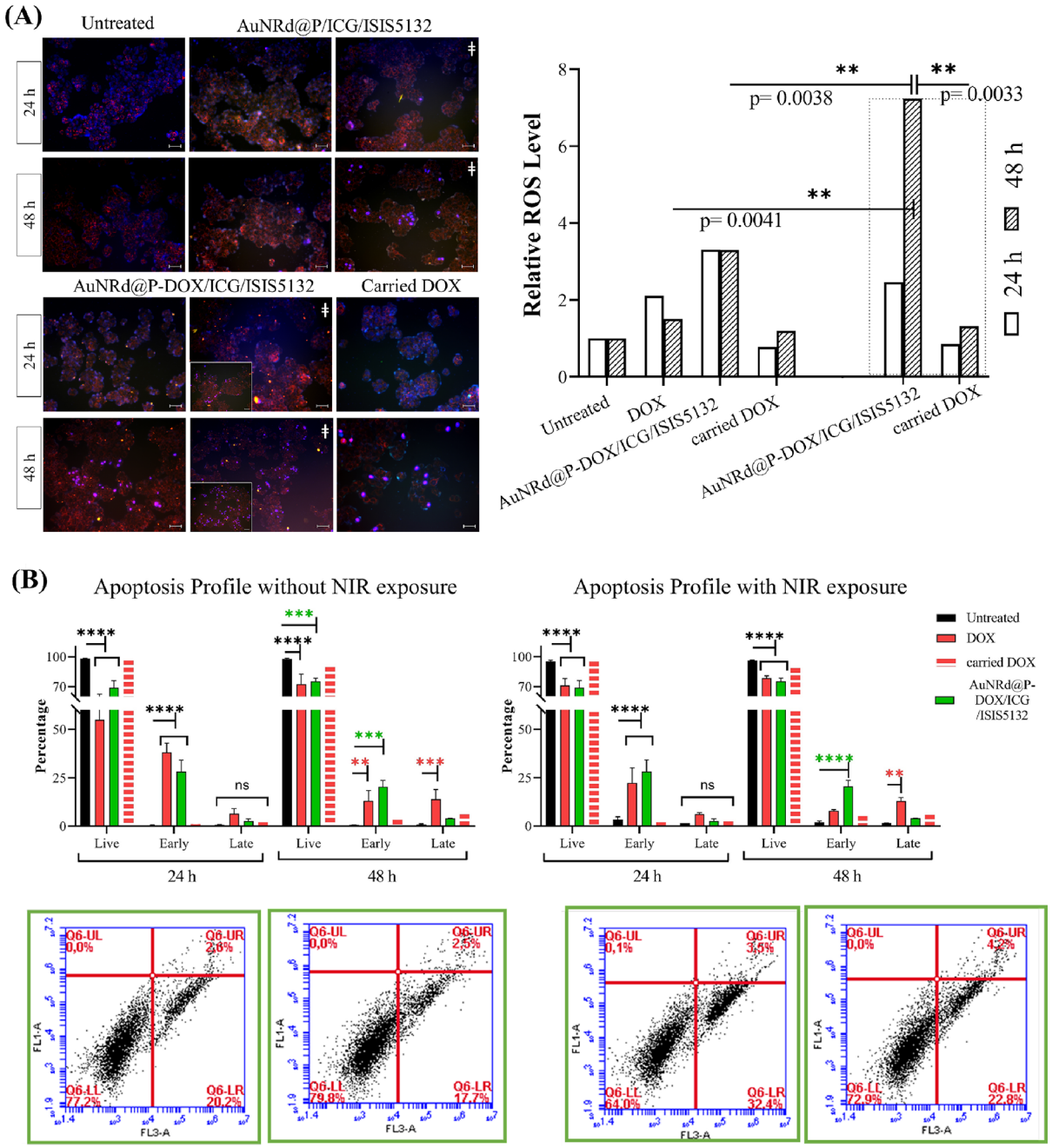

Figure 7. (A) Changes in intracellular ROS expression were detected by MitoSOX (red) as a superoxide indicator detected using an inverted microscope. After 24 and 48 h of treatment, untreated, AuNRd@P-DOX/ICG/ISIS5132, and carried DOX groups were compared with/without NIR exposure. The graph in the right panel shows the relative ROS level changes between groups. ROS production with NIR exposure increased over time. Black dashed line indicates NIR irradiated groups. Nucleus stained with DAPI (blue), nanoparticles that contain ISIS5132 oligonucleotide (conjugated with Cyanine-5 (Cy5)). Magnification 10× and insets 20×. Scale bar = 50 μm, h: hour, DOX: doxorubicin. (B) Flow cytometry analysis of annexin V/7"AAD staining of free DOX, AuNRd@P-DOX/ICG/ISIS5132, and carried DOX groups on MCF7 cells. The nanoparticle concentration was 3.9 μg/mL. The representative dot-plots were presented as the percentage of cells that were viable (Ann-V$^-$/7-AAD$^-$), early apoptotic (Ann-V$^+$/7-AAD$^-$), late apoptotic (Ann-V$^+$/7-AAD$^-$), and dead (Ann-V$^-$/7-AAD$^+$) for triple-acting nanoparticle (AuNRd@P-DOX/ICG/ISIS5132) with/without NIR exposure after treatment for 24 and 48 h, respectively, (shown in green frame). *p < 0.05, **p < 0.01, ****p < 0.0001.

increased the effects of NIR exposure, and similar relative protein expression changes for both nanoparticle groups were observed, although, statistically, AuNRd@P-DOX/ICG/ISIS5132 caused more significant cleavage of caspase-7 at 48 h of treatment even with/without NIR exposure when compared with the untreated group (p = 0.0374 and p = 0.0003, respectively), and total caspase-7 could also not be detected as well (Figure 6, left upper graph). To provide a more detailed evaluation, type I errors are also determined and adjusted p-values for all multiple comparisons were estimated (provided.pfzx file under the "Raw Statistics of Western Blot" name). After performing false discovery rate (FDR) methods from Benjamini and Hochberg,[26] we assessed the consistency of the previous significance of the increased cleaved-caspase-7

https://doi.org/10.1021/acsami.2c21180
ACS Appl. Mater. Interfaces 2023, 15, 9080−9098

level. We set our familywise alpha as 0.03. Notably, the AuNRd@P-DOX/ICG/ISIS5132 treatment at 24 and 48 h with NIR irradiation applied groups accepted the null hypothesis (q = 0.0229 and q = 0.0002, respectively), while the rest of the groups rejected it. In caspase3, relative protein expressions showed a decreased profile during nanoparticle treatments even though they did not show a significant impact statistically either through time or NIR irradiation (Figure 6, left middle graph). Similarly, the 0.97 μg/mL concentrations showed an increased cleavage of the caspase-7 protein level (p = 0.0049). Through time, NIR irradiation resulted in an increase in the cleaved caspase-7 relative protein expression level (p = 0.0008) (Figure 6). However, the FDR method rejected the null hypothesis. Nonetheless, a minimal change in the total caspase-3 was detected, but it did not provide a statistically significant change at the 0.97 μg/mL concentrations.

The final stage of the apoptotic orientation is the detection of PARP cleavage known as the hallmark of apoptosis.[49] For this particular reason, in assessing of the apoptotic protein patterns in MCF7 cells during treatments, we evaluated the PARP expression changes in our model. Higher nanoparticle concentration (3.9 μg/mL) showed significant changes when compared to untreated and carried DOX groups, and the impact increased over NIR exposure. When DOX free version of the nanoparticle (AuNRd@P/ICG/ISIS5132) administration was combined with NIR exposure, the total PARP cleaved significantly increased over time (p = 0.0368 for 24 h and p = 0.0061 for 48 h) by dual PTT/PDT. Remarkably, the AuNRd@P-DOX/ICG/ISIS5132 treatment revealed that the complete PARP cleavage enhanced with NIR exposure and presented statistically significant alterations through time (p = 0.0070 for both time intervals) and was found to be higher than the carried DOX group as well (p = 0.0259). Simultaneously, the total PARP could not be detected after 24 h of treatment. On the other hand, the 0.97 μg/mL concentration showed a similar effect at 24 h of treatment (p = 0.0083 without NIR and p = 0.0008 with NIR exposure). A noteworthy study has demonstrated the molecular interaction between PARP and caspase-7 and reported that caspase-7 maximizes the PARP cleavage by binding to its lysine residues from the N-terminal domain more efficiently than caspase-3.[51] Consistent with that study, here, we assumed that the increase in cleaved caspase-7 activations through our treatment model preferentially acted upon the PARP rather than the caspase-3. As is known, caspase-3 and caspase-7 are the effector caspases that act on both the intrinsic and extrinsic apoptosis pathways.[52]

Taken together, caspase-7 played a more prominent role than caspase-3 in our system. Previous studies showed that caspase-3 is a more dominant executioner caspase than caspase-7.[53] Yet, our observations of the nanoparticle administration process displayed a cell detachment profile due to the significant caspase-7 cleavage, and that also led to PARP activation. Moreover, the caspase-7 activation increases the sensitivity of the intrinsic apoptotic pathway and causes cells to detach from the attachment site.[54,55] Sequential treatments for cancer cells that aim at apoptotic cell death could trigger mitochondrial remodeling, cleavage of multiple proteins, and increased reactive oxygen species (ROS).[52] Therefore, during the course of cellular destruction by this synergistic effect of the chemo-/photo-thermal/photodynamic therapy, the differences in cellular detachment, cell shrinkage, and the loss of membrane integrity during cultivation were observed. We already ascertained cell detachment by motility assay (calcein-AM staining) before determining a valid reason for cell death. However, we used 3.9 μg/mL concentration after protein expression levels for ROS detection and apoptotic cellular profile accordingly.

With the ability of the triple acting, AuNRd@P-DOX/ICG/ISIS5132 and its DOX-free version AuNRd@P/ICG/ISIS5132 exhibited increased ROS production during intrinsic cell death (p = 0.0349 for both time intervals). Additionally, we found that the NIR exposure increased the impact of the AuNRd@P-DOX/ICG/ISIS5132 ROS production; particularly at 48 h of treatment, a significant increase was observed compared with its NIR exposure absent version (p = 0.0038), free DOX (IC_{50} level) (p = 0.0041), and carried DOX level (p = 0.0033). An increase in ROS production occurred when compared with or without NIR, and groups exhibited subcellular localization of the oxidation products resulting in their appearance inside the nuclei (Figure 7A and raw microscopy images were depicted in Figure S14). In contrast, the untreated group shows the basal level of mitochondrial oxidation products inside the cytoplasmic area. Moreover, it was evident in damaged cells that the nanoparticle treatments affected nuclear integrity, and NIR exposure most likely increased that response. Variations among treatments such as nanoparticles, drugs, and conjugated materials should be controlled against variation between independent replicates during experimental processes.[56,57] During our observations of this unique nanoparticle, we have given priority to maximizing the outcomes by using detailed statistical tests, and confirmative experiments accordingly. With all the experimental processes up to this point, we validated the efficacy of triple-acting nanoparticles (PTT, PDT, and chemotherapy) by decreased wound healing capacity and cell detachment by activation of particularly caspase-7 cleavage in particular, and this point led to a complete loss of the total PARP and simultaneously significant involvement of increased ROS levels. Although this whole process seems to have started well before 24 h, following uptake and NIR exposure to the cells, their activity continued over 48 h; then, we observed that the cell vitality/morphology almost terminated. To further support agreement with our findings, we validated the apoptotic cell profile by Annexin V staining and evaluated the outcome for untreated, free DOX (IC_{50} value), triple-acting nanoparticle AuNRd@P-DOX/ICG/ISIS5132, and the carried DOX concentration and compared with/without NIR irradiation for all groups (Figure S15).

Apoptotic profiles showed a decreased live-cell profile when compared with untreated and carried-DOX groups (p < 0.0001) with or without NIR exposure for the selected therapeutic concentration (3.9 μg/mL) over time as expected (Figure 7B). Furthermore, the late apoptosis profile showed no significant changes when compared with the untreated group, except for the free DOX group at 48 h (without NIR exposure the p-value was <0.0001; with NIR exposure p-value was 0.0039). Moreover, early apoptosis was also detected for the free-DOX group (p = 0.0030) as well. As is known, the late apoptosis is directly related to the necrotic cell death and we ascertained that avoiding necrosis was also achieved. Furthermore, the carried-DOX group did not cause any significant alterations to the apoptotic/necrotic behavior over time and NIR irradiation. On the other hand, the AuNRd@P-DOX/ICG/ISIS5132 showed a desired apoptotic profile, while necrosis was detected in less than 3% of the total cell profile.

https://doi.org/10.1021/acsami.2c21180
ACS Appl. Mater. Interfaces 2023, 15, 9080−9098

During the absence of NIR irradiation, triple-acting nanoparticles increased in the early apoptosis stage and continued to the 48 h mark ($p = 0.0005$ for 24 h and $p < 0.0001$ for 48 h of treatment). This outcome was also similar to the free DOX group's early apoptosis cell profile with no significant changes in other groups.

Regarding the action mechanisms of DOX, the nanoparticles exhibited the same apoptotic behavior without showing any necrosis. In contrast, the DOX concentration carried by the 3.9 μg/mL nanoparticle was 0.0848 μg/mL, which is 47.6 times less than the IC_{50} value of DOX. In terms of early apoptosis, the low amount of nanoparticles provided higher efficiency even without NIR exposure. When NIR was applied to the treatment system, the chemo-/photothermal/photodynamic therapy feature completed the action mechanism of the nanoparticles. The change in apoptotic cell profile becomes better than the free DOX group ($p < 0.0001$ for all time intervals). Given that apoptotic behavior is increased in a functional manner in MCF7 cells, triple-acting nanoparticles augmented the induction of apoptosis significantly only at 24 h of treatment when compared to the absence/presence of NIR application ($p = 0.0274$).

Comprehensively, our proposed nanoparticle system exhibits apoptotic cellular destructions. That process is already a highly coordinated molecular mechanism including sequential modifications.[54,58] Several activations, regulation processes, and outcomes of the MCF7 cell behavior *in vitro* through our treatment system were provided as clearly as possible. An important observation was made about detecting apoptotic cell profiles until flow cytometric analyses, namely that we could not determine the required time frame. As such, our treatment system was accompanied by decreased wound healing capacity, detachment from the surface, morphological disturbances, and activation of mainly caspase-7 and PARP and increased ROS production. We know that the concentration was sufficient but the required time course for therapeutic effects could not be determined. Until the last assay, we evaluated both time periods during the experiments. At the final stage, we confirmed a specific treatment time interval. The apoptotic cell profile detection by flow cytometry is sometimes viewed as a more or less passive assay than western blotting and may result in the absence of a correlation. This may also have prevented us from determining the treatment time frame. Selecting the efficient concentration after the western blotting stage was possible with statistical and overall evaluations, but the precise time interval was not. Only then, at 24 h of treatment with 3.9 μg/mL concentration maximized the outcome significantly while triplet activation has come into sight.

CONCLUSIONS

In this study, GLUT5-triggered-targeting nanoparticles were created to overcome monomodal therapy's limitations and to introduce effective chemo-/PDT/PTT synergistic therapy for breast cancer cells. Multifunctional phototherapeutic nanoparticles were developed, consisting of GLUT-targeted and DOX-conjugated glycopeptide polymer, ICG and active-targeted ISIS5132 ligand on the gold nanorods. The multifunctional sugar-decorated phototherapeutic nanoparticles were specifically uptaken by the cancer cells. Considering healthy cells, the uptake of the nanoparticles was not successful, and it did not show toxicity despite NIR irradiation. Administration of the multifunctional nanoparticles is targeted correctly and reveals very effective pH-dependent DOX release behavior, which is crucial for cancer therapy. Cellularly, that led to detachment and loss of motility. Subsequently, the capase-7 cleavage ascertained those deficiencies of the cancer cells. Moreover, phototherapeutic nanoparticles exhibited a very efficient PTT effect with 0.75 W/cm^2 NIR radiation, with their ability to convert NIR light to heat. Thus, the multifunctional phototherapeutic nanoparticles provided a significant PDT due to the ability to generate singlet oxygen, which is confirmed with the cleavage of PARP and increased ROS levels. Importantly, we showed that the phototherapeutic nanoparticles display a synergetic effect of the chemo-/photothermal/photodynamic therapy for selectively and targeted cancer therapy as an "all-in one" nanocarrier system. This study highlights the potential of AuNRd@P-DOX/ICG/ISIS5132 as a targeted-nanocarrier, particularly as a chemo-/PTT/PDT synergistic phototherapeutic system for breast cancer. Current efforts are focused on the *in vivo* evaluation of these promising biomaterials.

ASSOCIATED CONTENT

Supporting Information

The Supporting Information is available free of charge at https://pubs.acs.org/doi/10.1021/acsami.2c21180.

Analysis of GPC, ^{1}H-NMR, ATR-FTIR analysis of the synthesized polymers; and UV−vis data of AuNRds; detailed synthesized methods and characterization of precursor compounds and polymers; and *in vitro* detailed studies of photo- therapeutic nanoparticles (PDF)

AUTHOR INFORMATION

Corresponding Authors

Aydan Dag − *Department of Pharmaceutical Chemistry, Faculty of Pharmacy, Bezmialem Vakif University, Istanbul 34093, Turkey;* orcid.org/0000-0002-1552-8030; Email: adag@bezmialem.edu.tr

Gokcen Birlik Demirel − *Institute of Graduate Programs and Department of Chemistry, Polatlı Faculty of Arts and Sciences, Ankara Hacı Bayram Veli University, Ankara 06900, Turkey;* orcid.org/0000-0002-2057-8542; Email: gokcen.demirel@hbv.edu.tr

Authors

Busra Cetin Ersen − *Institute of Graduate Programs and Department of Chemistry, Polatlı Faculty of Arts and Sciences, Ankara Hacı Bayram Veli University, Ankara 06900, Turkey;* orcid.org/0000-0003-2522-2075

Beyza Goncu − *Experimental Research Center and Department of Medical Services and Techniques, Vocational School of Health Sciences, Bezmialem Vakif University, İstanbul 34093, Turkey*

Complete contact information is available at: https://pubs.acs.org/10.1021/acsami.2c21180

Author Contributions

The manuscript was written through contributions of all authors. All authors have given approval to the final version of the manuscript.

Notes

The authors declare no competing financial interest.

https://doi.org/10.1021/acsami.2c21180
ACS Appl. Mater. Interfaces 2023, 15, 9080−9098

■ ACKNOWLEDGMENTS

We thank Dr. Mehmet Ali Ergün (Gazi University) for useful discussions. This work is supported by the Scientific and Technological Research Council of Türkiye (grant no: 217Z063). The cancer cell image in the table of contents image and Scheme 1 was obtained from Shutterstock).

■ REFERENCES

(1) Fan, W.; Yung, B.; Huang, P.; Chen, X. Nanotechnology for multimodal synergistic cancer therapy. *Chem. Rev.* **2017**, *117*, 13566−13638.
(2) Ma, Y.; Huang, J.; Song, S.; Chen, H.; Zhang, Z. Cancer-targeted nanotheranostics: recent advances and perspectives. *Small* **2016**, *12*, 4936−4954.
(3) Shin, E.; Koo, J. S. Glucose metabolism and glucose transporters in breast cancer. *Front. Cell Dev. biol.* **2021**, *9*, No. 728759.
(4) Zhao, J.; Babiuch, K.; Lu, H.; Dag, A.; Gottschaldt, M.; Stenzel, M. H. Fructose-coated nanoparticles: a promising drug nanocarrier for triple-negative breast cancer therapy. *Chem. Commun.* **2014**, *50*, 15928−15931.
(5) Zhou, L.; Lu, R.; Liu, Q.; Xiao, B.; Hai, L.; Guo, L.; Wu, Y.; Zheng, Y. Two branched fructose modification improves tumor targeting delivery of liposomes to breast cancer in intro and in vivo. *J. Drug Delivery Sci. Technol.* **2021**, *61*, No. 102312.
(6) Fang, J.; Chen, Y.-C. Nanomaterials for photohyperthermia: a review. *Curr. Pharm. Des.* **2013**, *19*, 6622−6634.
(7) Yan, J.; Wang, C.; Jiang, X.; Wei, Y.; Wang, Q.; Cui, K.; Xu, X.; Wang, F.; Zhang, L. Application of phototherapeutic-based nanoparticles in colorectal cancer. *Int. J. Biol. Sci.* **2021**, *17*, 1361.
(8) Shen, S.; Tang, H.; Zhang, X.; Ren, J.; Pang, Z.; Wang, D.; Gao, H.; Qian, Y.; Jiang, X.; Yang, W. Targeting mesoporous silica-encapsulated gold nanorods for chemo-photothermal therapy with near-infrared radiation. *Biomaterials* **2013**, *34*, 3150−3158.
(9) Chen, W. H.; Yang, C. X.; Qiu, W. X.; Luo, G. F.; Jia, H. Z.; Lei, Q.; Wang, X. Y.; Liu, G.; Zhuo, R. X.; Zhang, X. Z. Multifunctional theranostic nanoplatform for cancer combined therapy based on gold nanorods. *Adv. Healthcare Mater.* **2015**, *4*, 2247−2259.
(10) Jia, Y.; Wang, X.; Hu, D.; Wang, P.; Liu, Q.; Zhang, X.; Jiang, J.; Liu, X.; Sheng, Z.; Liu, B. Phototheranostics: active targeting of orthotopic glioma using biomimetic proteolipid nanoparticles. *ACS Nano* **2019**, *13*, 386−398.
(11) Manchanda, R.; Fernandez-Fernandez, A.; Nagesetti, A.; McGoron, A. J. Preparation and characterization of a polymeric (PLGA) nanoparticulate drug delivery system with simultaneous incorporation of chemotherapeutic and thermo-optical agents. *Colloids Surf., B* **2010**, *75*, 260−267.
(12) Khazak, V.; Astsaturov, I.; Serebriiskii, I. G.; Golemis, E. A. Selective Raf inhibition in cancer therapy. *Expert Opin. Ther. Targets* **2007**, *11*, 1587−1609.
(13) (a) Eckhardt, S. G.; Rizzo, J.; Sweeney, K. R.; Cropp, G.; Baker, S. D.; Kraynak, M. A.; Kuhn, J. G.; Villalona-Calero, M. A.; Hammond, L.; Weiss, G. Phase I and pharmacologic study of the tyrosine kinase inhibitor SU101 in patients with advanced solid tumors. *J. Clin. Oncol.* **1999**, *17*, 1095−1095. (b) Roychowdhury, D.; Lahn, M. Antisense therapy directed to protein kinase C-alpha (Affinitak, LY900003/ISIS 3521): potential role in breast cancer. In *Seminars in oncology*, 2003; Elsevier: Vol. *30*, pp. 30−33.
(14) Kumar, R.; Wang, R.-A.; Bagheri-Yarmand, R. Emerging roles of MTA family members in human cancers. In *Seminars in oncology*, 2003; Elsevier: Vol. *30*, pp. 30−37.
(15) (a) Rudin, C. M.; Holmlund, J.; Fleming, G. F.; Mani, S.; Stadler, W. M.; Schumm, P.; Monia, B. P.; Johnston, J. F.; Geary, R.; Yu, R. Z.; Kwoh, T. J.; Dorr, F. A.; Ratain, M. J. Phase I trial of ISIS 5132, an antisense oligonucleotide inhibitor of c-raf-1, administered by 24-hour weekly infusion to patients with advanced cancer. *Clin. Cancer Res.* **2001**, *7*, 1214−1220. (b) Oza, A.; Elit, L.; Swenerton, K.; Faught, W.; Ghatage, P.; Carey, M.; McIntosh, L.; Dorr, A.; Holmlund, J.; Eisenhauer, E.; NCIC Clinical Trials Group Study (NCIC IND.116). Phase II study of CGP 69846A (ISIS 5132) in recurrent epithelial ovarian cancer: an NCIC clinical trials group study (NCIC IND. 116)☆. *Gynecol. Oncol.* **2003**, *89*, 129−133.
(16) Carboni, B.; Benalil, A.; Vaultier, M. Aliphatic amino azides as key building blocks for efficient polyamine syntheses. *J. Org. Chem.* **1993**, *58*, 3736−3741.
(17) Dag, A.; Cakilkaya, E.; Omurtag Ozgen, P. S.; Atasoy, S.; Yigit Erdem, G.; Cetin, B.; Çavuş Kokuroğlu, A.; Gurek, A. G. Phthalocyanine-conjugated glyconanoparticles for chemo-photodynamic combination therapy. *Biomacromolecules* **2021**, *22*, 1555−1567.
(18) Hernández, J. R.; Klok, H. A. Synthesis and ring-opening (co) polymerization of L-lysine N-carboxyanhydrides containing labile side-chain protective groups. *J. Polym. Sci., Part A: Polym. Chem.* **2003**, *41*, 1167−1187.
(19) Yi, Y.; Wang, H.; Wang, X.; Liu, Q.; Ye, M.; Tan, W. A smart, photocontrollable drug release nanosystem for multifunctional synergistic cancer therapy. *ACS Appl. Mater. Interfaces* **2017**, *9*, 5847−5854.
(20) Mazloomi-Rezvani, M.; Salami-Kalajahi, M.; Roghani-Mamaqani, H. "Grafting to" approach for surface modification of AuNPs with RAFT-mediated synthesized smart polymers: Stimuli-responsive behaviors of hybrid nanoparticles. *J. Phys. Chem. Solids* **2018**, *123*, 183−190.
(21) Hu, H.; Chen, J.; Yang, H.; Huang, X.; Wu, H.; Wu, Y.; Li, F.; Yi, Y.; Xiao, C.; Li, Y.; Tang, Y.; Li, Z.; Zhang, B.; Yang, X. Potentiating photodynamic therapy of ICG-loaded nanoparticles by depleting GSH with PEITC. *Nanoscale* **2019**, *11*, 6384−6393.
(22) Han, S.; Park, Y.-J.; Park, E.-J.; Kim, Y. T98G cell death induced by photothermal treatment with hollow gold nanoshell-coupled silica microrods prepared from Escherichia coli. *ACS Appl. Mater. Interfaces* **2019**, *11*, 8831−8837.
(23) Goncu, B.; Sevgi, E.; Kizilarslan Hancer, C.; Gokay, G.; Ozten, N. Differential anti-proliferative and apoptotic effects of lichen species on human prostate carcinoma cells. *PLoS One* **2020**, *15*, No. e0238303.
(24) Graph, Q.; Calculator, I. AAT Bioquest, Inc. *Sunnyvale, CA, USA:[(accessed on 20 May 2019)]. Available online:* https://www.aatbio. com/tools/linear-logarithmic-semi-log-regression-online-calculator.*[Google Scholar]*.
(25) Grishagin, I. V. Automatic cell counting with ImageJ. *Anal. Biochem.* **2015**, *473*, 63−65.
(26) Gerstung, M.; Papaemmanuil, E.; Campbell, P. J. Subclonal variant calling with multiple samples and prior knowledge. *Bioinformatics* **2014**, *30*, 1198−1204.
(27) Zamora-León, S. P.; Golde, D. W.; Concha, I. I.; Rivas, C. I.; Delgado-López, F.; Baselga, J.; Nualart, F.; Vera, J. C. Expression of the fructose transporter GLUT5 in human breast cancer. *Proc. Natl. Acad. Sci.* **1996**, *93*, 1847−1852.
(28) Rayavarapu, R. G.; Petersen, W.; Hartsuiker, L.; Chin, P.; Janssen, H.; Van Leeuwen, F. W.; Otto, C.; Manohar, S.; Van Leeuwen, T. G. In vitro toxicity studies of polymer-coated gold nanorods. *Nanotechnology* **2010**, *21*, No. 145101.
(29) Cunningham, C. C.; Holmlund, J. T.; Schiller, J. H.; Geary, R. S.; Kwoh, T. J.; Dorr, A.; Nemunaitis, J. A phase I trial of c-Raf kinase antisense oligonucleotide ISIS 5132 administered as a continuous intravenous infusion in patients with advanced cancer. *Clin. Cancer Res.* **2000**, *6*, 1626−1631.
(30) Kumari, A.; Kumari, K.; Gupta, S. The effect of nano-encapsulation of ICG on two-photon bioimaging. *RSC Adv.* **2019**, *9*, 18703−18712.
(31) Xu, W.; Qian, J.; Hou, G.; Wang, Y.; Wang, J.; Sun, T.; Ji, L.; Suo, A.; Yao, Y. PEGylated hydrazided gold nanorods for pH-triggered chemo/photodynamic/photothermal triple therapy of breast cancer. *Acta Biomater.* **2018**, *82*, 171−183.
(32) Kato, Y.; Ozawa, S.; Miyamoto, C.; Maehata, Y.; Suzuki, A.; Maeda, T.; Baba, Y. Acidic extracellular microenvironment and cancer. *Cancer Cell Int.* **2013**, *13*, 1−8.
(33) Yuan, H.; Fales, A. M.; Vo-Dinh, T. TAT peptide-functionalized gold nanostars: enhanced intracellular delivery and efficient

NIR photothermal therapy using ultralow irradiance. *J. Am. Chem. Soc.* **2012**, *134*, 11358−11361.
(34) Pang, X.; Wang, J.; Tan, X.; Guo, F.; Lei, M.; Ma, M.; Yu, M.; Tan, F.; Li, N. Dual-modal imaging-guided theranostic nanocarriers based on indocyanine green and mTOR inhibitor rapamycin. *ACS Appl. Mater. Interfaces* **2016**, *8*, 13819−13829.
(35) Tian, Q.; Jiang, F.; Zou, R.; Liu, Q.; Chen, Z.; Zhu, M.; Yang, S.; Wang, J.; Wang, J.; Hu, J. Hydrophilic Cu9S5 nanocrystals: a photothermal agent with a 25.7% heat conversion efficiency for photothermal ablation of cancer cells in vivo. *ACS Nano* **2011**, *5*, 9761−9771.
(36) Deng, L.; Cai, X.; Sheng, D.; Yang, Y.; Strohm, E. M.; Wang, Z.; Ran, H.; Wang, D.; Zheng, Y.; Li, P.; Shang, T.; Ling, Y.; Wang, F.; Sun, Y. A laser-activated biocompatible theranostic nanoagent for targeted multimodal imaging and photothermal therapy. *Theranostics* **2017**, *7*, 4410.
(37) Jiang, X.; Du, B.; Huang, Y.; Yu, M.; Zheng, J. Cancer photothermal therapy with ICG-conjugated gold nanoclusters. *Bioconjugate Chem.* **2020**, *31*, 1522−1528.
(38) Shen, F.; Chu, S.; Bence, A. K.; Bailey, B.; Xue, X.; Erickson, P. A.; Montrose, M. H.; Beck, W. T.; Erickson, L. C. Quantitation of doxorubicin uptake, efflux, and modulation of multidrug resistance (MDR) in MDR human cancer cells. *J. Pharmacol. Exp. Ther.* **2008**, *324*, 95−102.
(39) Luis, C.; Castaño-Guerrero, Y.; Soares, R.; Sales, G.; Fernandes, R. Avoiding the interference of doxorubicin with MTT measurements on the MCF-7 breast cancer cell line. *Methods Protoc.* **2019**, *2*, 29.
(40) Kauanova, S.; Urazbayev, A.; Vorobjev, I. The frequent sampling of wound scratch assay reveals the "opportunity" window for quantitative evaluation of cell motility-impeding drugs. *Front. Cell Dev. biol.* **2021**, *9*, No. 640972.
(41) Wang, X.; Decker, C. C.; Zechner, L.; Krstin, S.; Wink, M. In vitro wound healing of tumor cells: inhibition of cell migration by selected cytotoxic alkaloids. *BMC Pharmacol. Toxicol.* **2019**, *20*, 1−12.
(42) Stamm, A.; Reimers, K.; Strauß, S.; Vogt, P.; Scheper, T.; Pepelanova, I. In vitro wound healing assays−state of the art. *BioNanoMaterials* **2016**, *17*, 79−87.
(43) Huang, C.; Becker, M. F.; Keto, J. W.; Kovar, D. Annealing of nanostructured silver films produced by supersonic deposition of nanoparticles. *J. Appl. Phys.* **2007**, *102*, No. 054308.
(44) Braut-Boucher, F.; Pichon, J.; Rat, P.; Adolphe, M.; Aubery, M.; Font, J. A non-isotopic, highly sensitive, fluorimetric, cell-cell adhesion microplate assay using calcein AM-labeled lymphocytes. *J. Immunol. Methods* **1995**, *178*, 41−51.
(45) Bratosin, D.; Mitrofan, L.; Palii, C.; Estaquier, J.; Montreuil, J. Novel fluorescence assay using calcein-AM for the determination of human erythrocyte viability and aging. *Cytometry, Part A* **2005**, *66*, 78−84.
(46) Opas, M.; Dziak, E. Intracellular pH and pCa measurement. *Confocal Microscopy Methods Protoc.* **1998**, 305−313.
(47) Miles, F. L.; Lynch, J. E.; Sikes, R. A. Cell-based assays using calcein acetoxymethyl ester show variation in fluorescence with treatment conditions. *J. Biol. Methods* **2015**, *2*, No. e29.
(48) Mooney, L.; Al-Sakkaf, K.; Brown, B.; Dobson, P. Apoptotic mechanisms in T47D and MCF-7 human breast cancer cells. *Br. J. Cancer* **2002**, *87*, 909−917.
(49) Pillai-Kastoori, L.; Schutz-Geschwender, A. R.; Harford, J. A. A systematic approach to quantitative Western blot analysis. *Anal. Biochem.* **2020**, *593*, No. 113608.
(50) Zhang, K.; Fan, W.; Chen, D.; Jiang, L.; Li, Y.; Yao, Z.; Yang, Y.; Qiu, D. Selection and validation of reference genes for quantitative gene expression normalization in Taxus spp. *Sci. Rep.* **2020**, *10*, 1−10.
(51) Boucher, D.; Blais, V.; Denault, J.-B. Caspase-7 uses an exosite to promote poly (ADP ribose) polymerase 1 proteolysis. *Proc. Natl. Acad. Sci.* **2012**, *109*, 5669−5674.
(52) Weber, T. G.; Pöschinger, T.; Galbán, S.; Rehemtulla, A.; Scheuer, W. Noninvasive monitoring of pharmacodynamics and kinetics of a death receptor 5 antibody and its enhanced apoptosis induction in sequential application with doxorubicin. *Neoplasia* **2013**, *15*, 863−874.
(53) Brentnall, M.; Rodriguez-Menocal, L.; De Guevara, R. L.; Cepero, E.; Boise, L. H. Caspase-9, caspase-3 and caspase-7 have distinct roles during intrinsic apoptosis. *BMC Cell Biol.* **2013**, *14*, 1−9.
(54) Jelínek, M.; Balušíková, K.; Schmiedlová, M.; Němcová-Fürstová, V.; Šrámek, J.; Stančíková, J.; Zanardi, I.; Ojima, I.; Kovář, J. The role of individual caspases in cell death induction by taxanes in breast cancer cells. *Cancer Cell Int.* **2015**, *15*, 1−16.
(55) Narla, G.; Sangodkar, J.; Ryder, C. B. The impact of phosphatases on proliferative and survival signaling in cancer. *Cell. Mol. Life Sci.* **2018**, *75*, 2695−2718.
(56) Anson, F.; Thayumanavan, S.; Hardy, J. A. Exogenous introduction of initiator and executioner caspases results in different apoptotic outcomes. *JACS Au* **2021**, *1*, 1240−1256.
(57) Yan, C.; Wang, H.; Boyd, D. D. ATF3 represses 72-kDa type IV collagenase (MMP-2) expression by antagonizing p53-dependent trans-activation of the collagenase promoter. *J. Biol. Chem.* **2002**, *277*, 10804−10812.
(58) Carneiro, B. A.; El-Deiry, W. S. Targeting apoptosis in cancer therapy. *Nat. Rev. Clin. Oncol.* **2020**, *17*, 395−417.

https://doi.org/10.1021/acsami.2c21180
ACS Appl. Mater. Interfaces 2023, 15, 9080−9098